

# Evolution of the Velocity Dispersion of Self-Gravitating Particles in Disc Potentials

Kouji Shiidsuka and Shigeru Ida

*Department of Earth and Planetary Sciences, Faculty of Science, Tokyo Institute of Technology, Tokyo 152-8551, Japan*  
E-mail: kshiidsu@geo.titech.ac.jp

7 October 2018

## ABSTRACT

The ratio of the vertical velocity dispersion to radial one ( $\sigma_z/\sigma_R$ ) of self-gravitating bodies in various disc potentials is investigated through two different numerical methods (statistical compilation of two-body encounters and  $N$ -body simulations). The velocity dispersion generated by two-body relaxation is considered. The ratio is given as a function of a disc potential parameter,  $\kappa/\Omega$ , where  $\kappa$  and  $\Omega$  are the epicycle and circular frequencies (the parameters  $\kappa/\Omega = 1$  and  $2$  correspond to Kepler rotation and solid-body rotation). For  $1 \leq \kappa/\Omega \lesssim 1.5$ , the velocity dispersion increases keeping some anisotropy ( $\sigma_z/\sigma_R \sim 0.5\text{--}0.7$ ) if the amplitude of radial excursion is larger than tidal radius, while  $\sigma_z/\sigma_R \ll 1$  for smaller amplitude. On the other hand, for  $1.5 \lesssim \kappa/\Omega \leq 2.0$ , we found isotropic state ( $\sigma_z/\sigma_R \simeq 1$ ) in the intermediate velocity regime, while anisotropic state ( $\sigma_z/\sigma_R < 1$ ) still exists for higher and lower velocity regimes. The range of the intermediate velocity regime expands with  $\kappa/\Omega$ . In the limit of solid-body rotation, the regime covers all over the velocity space. Thus, the velocity dispersion generally has two different anisotropic states for each disc potential ( $1 \leq \kappa/\Omega < 2$ ) and one isotropic state for  $1.5 \lesssim \kappa/\Omega < 2$  where the individual states correspond to different amplitude of velocity dispersion, while in the limit of solid-body rotation ( $\kappa/\Omega = 2.0$ ), entire velocity space is covered by the isotropic state.

**Key words:** celestial mechanics, stellar dynamics – Galaxy: solar neighbourhood – methods: numerical – galaxies: kinematics and dynamics

## 1 INTRODUCTION

Gravitational interactions between bodies in a disc potential tend to increase velocity dispersion of the bodies as well as diffuse the bodies radially. The increased random energy is transferred from the potential energy through the radial diffusion. This process is called ‘disc heating’ for stars and molecular clouds in the Galactic gravitational field (e.g. Spitzer & Schwarzschild 1953; Binney & Tremaine 1987; Lacey 1991), and ‘viscous stirring’ for planetesimals in the protoplanetary disc or ring particles around planets (e.g. Stewart & Wetherill 1988; Ida 1990). Hereafter we use ‘disc heating’. In general, disc heating results in anisotropic velocity dispersion. The radial and the vertical components of the velocity dispersion ( $\sigma_R$  and  $\sigma_z$ ) evolve with keeping a certain ‘equilibrium’ ratio, which is not generally unity.

Ida & Makino (1992) showed through  $N$ -body simulations that  $\sigma_z/\sigma_R \simeq 0.45$  for self-gravitating planetesimals in the solar (Keplerian) potential. Numerical simulations of disc stars perturbed by massive molecular clouds in the solar neighbourhood showed  $\sigma_z/\sigma_R \simeq 0.6$  (Villumsen 1985; Kokubo & Ida 1992). Observations of stars in the so-

lar neighbourhood show consistent anisotropy (e.g., Wielen 1977; Chen, Asai, Figueras & Torra 1997).

In our galaxy, collective effects such as transient density waves would play an important role in velocity dispersion of stars in the solar neighbourhood (e.g., Barbanis & Woltjer 1967; Binney & Lacey 1988; Jenkins & Binney 1990). Nevertheless, it is important to clarify velocity dispersion created by (non-collective) two-body relaxation in a disc potential, because the two-body relaxation is one of the most basic processes in a self-gravitating disc system. Even if the collective effects dominate the disc heating in our galaxy, it is important to understand a competitive process, the heating by two-body relaxation. Furthermore, the two-body relaxation may dominate in the central region of our galaxy or in other galaxies. In the present paper, we are concerned with dynamics regulated by the two-body relaxation in an ‘idealized’ disc system with the potential characterized by a parameter  $\kappa/\Omega$ , where  $\kappa$  and  $\Omega$  are horizontal epicycle frequency (see Eqs. (5)) and circular frequency of the disc potential, which indicates radial dependence of a disc potential.

It is suggested that the equilibrium ratio ( $\sigma_z/\sigma_R$ )

arXiv:astro-ph/9907243v1 19 Jul 1999

depends on  $\kappa/\Omega$ . Lacey(1984) and Ida, Kokubo & Makino(1993) (hereafter IKM93) analytically investigated the equilibrium value of  $\sigma_z/\sigma_R$  as a function of  $\kappa/\Omega$ . They assumed that the evolution of the velocity dispersion is described by the sum of many independent two-body scatterings in a disc potential with various initial conditions. They adopted the epicycle approximation (e.g. Binney & Tremaine 1987) and calculated orbital changes with the impulse approximation neglecting the external disc potential. IKM93 also suggested that the anisotropy is produced by deceleration of horizontal velocity at close approach due to shear motion (see section 2.2). For the Keplerian potential ( $\kappa/\Omega = 1$ ) and the galactic potential in the solar neighbourhood ( $\kappa/\Omega \simeq 1.4$ ), IKM93 obtained the value of  $\sigma_z/\sigma_R$  that are consistent with  $N$ -body simulations (and observations), while Lacey(1984) show significantly large values (Fig. 1). IKM93 claimed that choice of the maximum impact parameter in the two-body formulae affects the equilibrium value of  $\sigma_z/\sigma_R$ . IKM93 carefully chose the maximum impact parameter comparing with numerical orbital integration to obtain smaller  $\sigma_z/\sigma_R$  than that of Lacey(1984). However, IKM93 obtained  $\sigma_z/\sigma_R \neq 1$  in the limit of  $\kappa/\Omega = 2$  (solid-body rotation). It would be reasonable to consider  $\sigma_z/\sigma_R = 1$  in the solid-body rotation, since shear motion vanishes. Lacey(1984) gave an argument with Jeans theorem to show  $\sigma_z/\sigma_R = 1$  in that case. Lacey(1984) obtained  $\sigma_z/\sigma_R = 1$  for  $\kappa/\Omega = 2$ , which is consistent with the above argument, although he failed to reproduce consistent values of  $\sigma_z/\sigma_R$  for smaller  $\kappa/\Omega$ . Things have been obscured because of the lack of both observation and numerical work in the limiting case,  $\kappa/\Omega \simeq 2$ .

To address this problem, we performed numerical simulations in disc potentials with wide range of  $\kappa/\Omega$  up to  $\sim 2$ . In section 2, we calculate the disc heating as the sum of many independent two-body scatterings in a disc potential, as Lacey(1984) and IKM93 did, but orbital changes are obtained by numerical orbital integrations. Our numerical calculations show an isotropic-dispersion ( $\sigma_z/\sigma_R \sim 1$ ) regime in velocity space if  $\kappa/\Omega \gtrsim 1.5$ . We also found that the range of the regime expands with  $\kappa/\Omega$  and the regime dominates all over the velocity space in the limiting case of the solid-body rotation ( $\kappa/\Omega = 2$ ).

In section 3, to confirm our results obtained in section 2, we performed  $N$ -body simulations of particles in various disc potentials. The results in section 2 and 3 are in good agreement with each other. In section 4, we summarize our results.

## 2 VELOCITY EVOLUTION DUE TO MANY TWO-BODY SCATTERINGS IN DISC POTENTIALS

### 2.1 Basic Formulation

In this section, we consider a swarm of test bodies (particle 1) gravitationally perturbed by field bodies (particle 2) in a disc potential field. We evaluate change rate of the velocity dispersion of the test bodies by statistically compiling the velocity changes in individual two-body encounters with field bodies, which are calculated numerically, following the method adopted by Ida (1990) and Kokubo & Ida (1992). Here we are also concerned with the cases with  $\kappa/\Omega$  close to

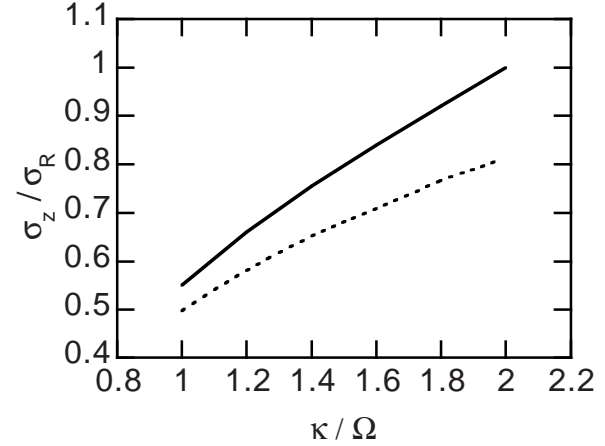


**Figure 1.** The equilibrium ratio  $\sigma_z/\sigma_R$  as a function of  $\kappa/\Omega$  obtained by Lacey(1984) (solid line) and IKM93 (dotted line). Since the result of IKM93 is weakly dependent on the disc scale height owing to their choice of  $\ln \Lambda$ , we plot the case in which the disc scale height is larger than the tidal radius of a particle where their assumption is valid (the case where  $\langle i_*^2 \rangle^{1/2} = 5$ , see section 2).

2 while Ida (1990) and Kokubo & Ida (1992) only studied the cases with  $\kappa/\Omega = 1.0$  and 1.39.

We assume that 'background bodies' generating the disc potential is continuously distributed and they do not contribute to two-body scattering.

We adopt the epicycle approximation (see e.g. Petit & Hénon 1986; Binney & Tremaine 1987): the velocity dispersion is sufficiently smaller than rotational velocity around galactic centre. We use the following rotating coordinates:

$$\begin{cases} x = (R - a)/r_g, \\ y = (a\phi - a\Omega t)/r_g, \\ z = z/r_g, \end{cases} \quad (1)$$

where  $(R, \phi, z)$  are cylindrical coordinates centred at the bottom of the disc potential,  $\Omega$  is the circular frequency at  $R = a$ . The normalization factor  $r_g$  is defined by

$$r_g = \left( \frac{G(m_1 + m_2)}{\Omega^2} \right)^{\frac{1}{3}}, \quad (2)$$

where  $m_1$  and  $m_2$  are the masses of the particle 1 and 2 and  $G$  is the gravitational constant. The radius  $r_g$  corresponds to tidal radius within a numerical factor of  $O(1)$  except for  $\kappa/\Omega \simeq 2$  (see Eq. (21))

In the epicycle approximation, the unperturbed orbits are given by (Petit & Hénon 1986; Binney & Tremaine 1987)

$$\begin{cases} x_j = b_j - e_j \frac{\Omega}{\kappa} \cos\left(\frac{\kappa}{\Omega}t - \tau_j\right), \\ y_j = \lambda_j - \frac{\alpha}{2} b_j t + 2e_j \frac{\Omega^2}{\kappa^2} \sin\left(\frac{\kappa}{\Omega}t - \tau_j\right), \\ z_j = i_j \frac{\Omega}{\nu} \sin\left(\frac{\nu}{\Omega}t - \omega_j\right), \end{cases} \quad (3)$$

and

$$\begin{cases} \dot{x}_j = e_j \sin\left(\frac{\kappa}{\Omega}t - \tau_j\right), \\ \dot{y}_j = -\frac{\alpha}{2} b_j + 2e_j \frac{\Omega}{\kappa} \cos\left(\frac{\kappa}{\Omega}t - \tau_j\right), \\ \dot{z}_j = i_j \cos\left(\frac{\nu}{\Omega}t - \omega_j\right), \end{cases} \quad (4)$$

where time is scaled by  $\Omega^{-1}$ , and  $\kappa$  and  $\nu$  are epicycle frequency and frequency of vertical oscillation which are defined by

$$\begin{cases} \kappa = \left( \frac{\partial^2 \Phi}{\partial R^2} \right)_{R=a} + 3\Omega^2 = 2\Omega \left( R \frac{\partial \Omega}{\partial R} \right)_{R=a}, \\ \nu = \left( \frac{\partial^2 \Phi}{\partial z^2} \right)_{R=a}, \end{cases} \quad (5)$$

where  $\Phi(R, z)$  is an axisymmetric disc potential. For convenience, we introduced a parameter  $\alpha$  which indicates the strength of shear motion:

$$\alpha = 4 - \frac{\kappa^2}{\Omega^2}. \quad (6)$$

The quantities  $e$ ,  $i$ ,  $b$ ,  $\tau$ ,  $\omega$ , and  $\lambda$  are the constants of integration. Equations (3) and (4) represent the particle motion as a combination of planar epicycle and vertical oscillation around the guiding center rotating in a non-inclined circular orbit. The quantities  $e\Omega/\kappa$  and  $\tau$  are the amplitude and the phase of the horizontal oscillation, respectively. Similarly,  $i\Omega/\nu$  and  $\omega$  are those of the vertical oscillation. The first term of the right hand side of  $y_j$  represents the shear velocity,  $[\Omega(a + r_g b) - \Omega(a)]a$  scaled by  $r_g \Omega$  (we assumed  $br_g \ll a$ ). In the special case of Kepler rotation ( $\kappa/\Omega = 1.0$ ), the constants  $er_g/a$  and  $ir_g/a$  are called eccentricity and inclination.

From equations (4), rms velocity averaged over an epicycle period of  $j$ -th particle is given by

$$\begin{cases} \sigma_{jR} \equiv \bar{x}_j^2 \frac{1}{2} r_g \Omega = \frac{e_j}{\sqrt{2}} r_g \Omega, \\ \sigma_{jz} \equiv \bar{z}_j^2 \frac{1}{2} r_g \Omega = \frac{i_j}{\sqrt{2}} r_g \Omega, \end{cases} \quad (7)$$

where ' $\bar{\cdot}$ ' denotes time-averaging during the epicycle period. Then we define the velocity dispersion of a swarm of particle 1 (test bodies) as

$$\begin{cases} \sigma_R \equiv \frac{\langle e_1^2 \rangle^{1/2}}{\sqrt{2}} r_g \Omega, \\ \sigma_z \equiv \frac{\langle i_1^2 \rangle^{1/2}}{\sqrt{2}} r_g \Omega, \end{cases} \quad (8)$$

where ' $\langle \cdot \rangle$ ' denotes ensemble-averaging (i.e.  $\sigma_R = \langle \sigma_{1R}^2 \rangle^{1/2}$  and  $\sigma_z = \langle \sigma_{1z}^2 \rangle^{1/2}$ ). We also call  $\langle e_1^2 \rangle^{1/2}$  and  $\langle i_1^2 \rangle^{1/2}$  'normalized velocity dispersion' and pursue evolution of them. Kokubo & Ida (1992) considered gravitational scatterings of test bodies (disc stars) by many massive field bodies (giant molecular clouds) which are in non-inclined circular orbit. According to them, the evolution of the normalized velocity dispersion of the test bodies are given by

$$\begin{cases} \frac{d\langle e_1^2 \rangle}{dt} = n_{s2} r_g^2 \Omega \int f_1(e_1, i_1) P_{\text{heat}}(e_1, i_1) de_1^2 di_1^2, \\ \frac{d\langle i_1^2 \rangle}{dt} = n_{s2} r_g^2 \Omega \int f_1(e_1, i_1) Q_{\text{heat}}(e_1, i_1) de_1^2 di_1^2 \end{cases} \quad (9)$$

where

$$\begin{cases} P_{\text{heat}}(e, i) \equiv \int \Delta e^2 \frac{\alpha}{2} |b| \frac{d\tau d\omega}{(2\pi)^2} db = \int p(e, i, b) db, \\ Q_{\text{heat}}(e, i) \equiv \int \Delta i^2 \frac{\alpha}{2} |b| \frac{d\tau d\omega}{(2\pi)^2} db = \int q(e, i, b) db \end{cases} \quad (10)$$

(we assumed  $b$ ,  $\tau$ , and  $\omega$  are distributed randomly). The

quantities  $p(e, i, b)$  and  $q(e, i, b)$  are introduced for later convenience and written as

$$\begin{cases} p(e, i, b) \equiv \int \Delta e^2 \frac{\alpha}{2} |b| \frac{d\tau d\omega}{(2\pi)^2}, \\ q(e, i, b) \equiv \int \Delta i^2 \frac{\alpha}{2} |b| \frac{d\tau d\omega}{(2\pi)^2}. \end{cases} \quad (11)$$

In Eqs. (9),  $n_{s2}$  is the surface number density of the massive bodies and  $f_1$  is the velocity distribution of the test bodies, which is normalized as

$$\int f_1(e, i) de^2 di^2 = 1. \quad (12)$$

Equations (9) are valid when  $m_2 \gg m_1$ . In more general case where the mass of a test body (particle 1) is comparable to that of a field body (particle 2), Eqs. (9) are revised as

$$\begin{cases} \frac{d\langle e_1^2 \rangle}{dt} = n_{s2} r_g^2 \Omega \left( \frac{m_2}{m_1 + m_2} \right)^2 \langle P_{\text{heat}} \rangle, \\ \frac{d\langle i_1^2 \rangle}{dt} = n_{s2} r_g^2 \Omega \left( \frac{m_2}{m_1 + m_2} \right)^2 \langle Q_{\text{heat}} \rangle, \end{cases} \quad (13)$$

where

$$\begin{cases} \langle P_{\text{heat}} \rangle = \int f(e, i) P_{\text{heat}}(e, i) de^2 di^2, \\ \langle Q_{\text{heat}} \rangle = \int f(e, i) Q_{\text{heat}}(e, i) de^2 di^2 \end{cases} \quad (14)$$

(Ohtsuki 1998, Stewart & Ida 1998). In Eqs. (14),  $e$  and  $i$  are velocity dispersion of the relative motion defined by

$$\begin{cases} e \cos \tau = e_2 \cos \tau_2 - e_1 \cos \tau_1, \\ e \sin \tau = e_2 \sin \tau_2 - e_1 \sin \tau_1, \\ i \cos \omega = i_2 \cos \omega_2 - i_1 \cos \omega_1, \\ i \sin \omega = i_2 \sin \omega_2 - i_1 \sin \omega_1. \end{cases} \quad (15)$$

Then, we obtain

$$\begin{cases} \langle e^2 \rangle = \langle e_1^2 \rangle + \langle e_2^2 \rangle, \\ \langle i^2 \rangle = \langle i_1^2 \rangle + \langle i_2^2 \rangle. \end{cases} \quad (16)$$

Under an assumption that both  $f_1$  and  $f_2$  (velocity distributions of particles 1 and 2) are Rayleigh distribution,  $f$  is again Rayleigh distribution (Ohtsuki 1998, Stewart & Ida 1998):

$$\begin{aligned} f(e, i) de^2 di^2 &= \frac{1}{\langle e^2 \rangle \langle i^2 \rangle} \exp \left( -\frac{e^2}{\langle e^2 \rangle} - \frac{i^2}{\langle i^2 \rangle} \right) de^2 di^2 \\ &= \frac{4ei}{\langle e^2 \rangle \langle i^2 \rangle} \exp \left( -\frac{e^2}{\langle e^2 \rangle} - \frac{i^2}{\langle i^2 \rangle} \right) dedi. \end{aligned} \quad (17)$$

Equations (13) and (14) imply that  $\langle P_{\text{heat}} \rangle$  and  $\langle Q_{\text{heat}} \rangle$ , which are calculated only by orbital change in the relative motion, determine the ratio of the velocity dispersion. It should be noted that integration with  $i$  in Eqs. (14) is also equivalent to that with  $v_z$  and  $z$ , i.e., averaging with vertical velocity and height from disk mid-plane (Lissauer & Stewart 1993). Strictly speaking, Eq. (13) should include the terms expressing recoil of dynamical friction, which is proportional to  $(m_1 \langle e_2^2 \rangle - m_2 \langle e_1^2 \rangle)$  or  $(m_1 \langle i_2^2 \rangle - m_2 \langle i_1^2 \rangle)$  (Ohtsuki 1998; Stewart & Ida 1998), however, we neglect it, assuming the energy equipartition between particles 1 and 2 is already realized. In this case, it is shown that the recoil terms are much smaller than the heating terms (right hand sides of Eqs. (13)) if  $m_1 \ll m_2$  (Ida 1990). Furthermore, in the identical particle case, Eq.(13) is exact.

The equations of the relative motion are given by (e.g. Icke 1982; Petit & Hénon 1986; Kokubo & Ida 1992)

$$\begin{cases} \ddot{x} - 2\dot{y} &= \alpha x & -x/r^3, \\ \ddot{y} + 2\dot{x} &= & -y/r^3, \\ \ddot{z} &= -(\nu/\Omega)^2 z & -z/r^3, \end{cases} \quad (18)$$

where time is scaled by  $\Omega^{-1}$ ,  $(x, y, z) = (x_2 - x_1, y_2 - y_1, z_2 - z_1)$ , and  $r$  is scaled distance,  $r = (x^2 + y^2 + z^2)^{1/2}$ . The last terms on the right hand side of Eqs. (18) represent the gravitational interaction between two particles. Since we scale length and time by  $r_g$  and  $\Omega$ ,  $G(m_1 + m_2)x/r^3$  is reduced to  $x/r^3$  in these equations. The terms  $-2\dot{y}$  and  $2\dot{x}$  are the Coriolis force. In the case of  $\kappa/\Omega = 1.0$  and  $\nu/\Omega = 1.0$ , Eqs. (18) are called Hill's equations which describe motion in the Kepler potential.

We will numerically integrate Eqs. (18) to evaluate the changes of orbital elements, in particular,  $e$  and  $i$ . The relative orbital elements are related to relative motion  $(x, y, z, \dot{x}, \dot{y}, \dot{z})$  in a similar way to Eqs. (3) and (4) as

$$\begin{cases} x = b - e \frac{\Omega}{\kappa} \cos(\frac{\kappa}{\Omega} t - \tau), \\ y = \lambda - \frac{\alpha}{2} b t + 2e \frac{\Omega^2}{\kappa^2} \sin(\frac{\kappa}{\Omega} t - \tau), \\ z = i \frac{\Omega}{\nu} \sin(\frac{\nu}{\Omega} t - \omega), \end{cases} \quad (19)$$

and

$$\begin{cases} \dot{x} = e \sin(\frac{\kappa}{\Omega} t - \tau), \\ \dot{y} = -\frac{\alpha}{2} b + 2e \frac{\Omega}{\kappa} \cos(\frac{\kappa}{\Omega} t - \tau), \\ \dot{z} = i \cos(\frac{\nu}{\Omega} t - \omega). \end{cases} \quad (20)$$

When the two particles are so far away that the mutual gravitational terms in Eqs. (18) are negligible, the relative orbital elements are constants. When they approach each other, the orbital elements change through the mutual perturbation. We show the examples of unperturbed motion, i.e., the motion with constant orbital elements in Fig. 2. In this figure,  $\kappa/\Omega = 1.87$ ,  $e = 1.0$ , and  $b = 1.0$  (solid line), 3.0 (dotted line), and 5.0 (dashed line).

## 2.2 Numerical Results of $P_{\text{heat}}$ and $Q_{\text{heat}}$

We first investigate the behaviour of the 'elementary' quantities  $P_{\text{heat}}$  and  $Q_{\text{heat}}$  (Eqs. (10)) since they show clearer physical properties than  $\langle P_{\text{heat}} \rangle$  and  $\langle Q_{\text{heat}} \rangle$  and the averaging (Eqs. (14)) will not change the ratio of the velocity dispersion substantially.

To obtain  $P_{\text{heat}}$  ( $Q_{\text{heat}}$ ), we calculate  $\Delta e^2$  ( $\Delta i^2$ ) with various sets of  $(b, \tau, \omega)$  through orbital integration for each set of  $(e, i)$ , following Ida (1990) and Kokubo & Ida (1992). As described in the previous subsection, only relative motion which obeys Eqs. (18) is calculated.

When relative distance  $r$  is large enough that mutual gravitation can be neglected, the orbital elements  $(e, i, b, \tau, \omega, \lambda)$  are constants. We start our orbital integration with sufficiently large  $y$ . A body approaches the other owing to shear motion. During the encounter, the orbital elements are changed by mutual gravitational perturbation. We stop the integration when  $|y|$  becomes large enough again. Changes of the orbital elements are determined as the difference between orbital elements of initial and final states, i.e.,

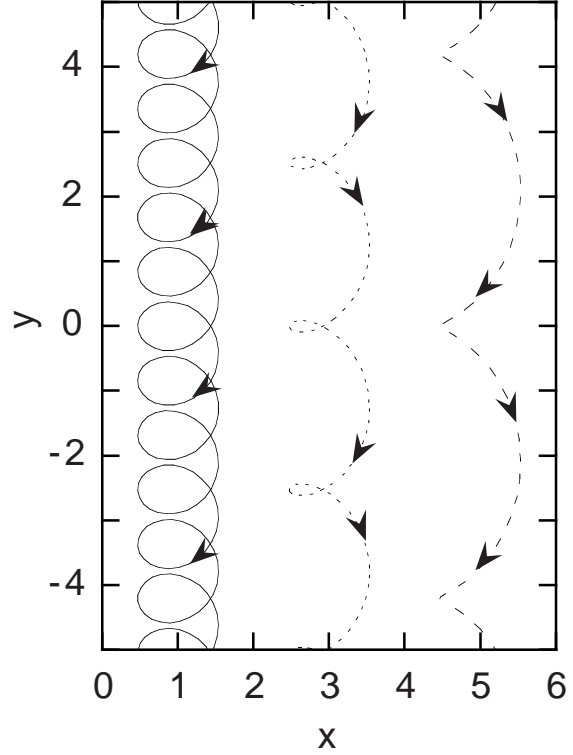


**Figure 2.** Examples of the unperturbed orbit on the  $x$ - $y$  plane. For all cases,  $e = 1.0$  and  $\kappa/\Omega = 1.87$ . Solid, dotted, and dashed lines are orbits with  $b = 1.0$ ,  $b = 3.0$ , and  $b = 5.0$ , respectively.

$\Delta e^2 = e_{\text{final}}^2 - e_{\text{initial}}^2$ . Since contribution in the integral (10) from non-crossing distant encounters rapidly decreases with  $|b|$  in a disc system (Ida 1990; Hasegawa & Nakazawa 1990; Kokubo & Ida 1992), initial  $b$  of orbits we calculated is confined in some finite regime. Furthermore, according to the symmetry of basic equations, the changes of  $e^2$  and  $i^2$  take the same values for the orbits with  $b$  and  $-b$  and those with  $\omega$  and  $\omega + \pi$ . Hence, we calculated orbits with  $0 < b \leq b_{\text{max}}$ ,  $0 \leq \omega \leq \pi$ , and  $-\pi \leq \tau \leq \pi$  (for the value of  $b_{\text{max}}$ , see below).

The orbits are integrated with the fourth-order Hermite scheme (Makino & Aarseth 1992). We also employed the algorithm developed by Emori, Ida, & Nakazawa (1993), where the part of deviation from the unperturbed epicycle orbit is numerically calculated while the part of the unperturbed epicycle orbit is analytically calculated.

We numerically calculated the heating rates with various  $\kappa/\Omega$ :  $\kappa/\Omega = 1.00, 1.30, 1.58, 1.73$ , and  $1.87$ . Since IKM93 showed that anisotropy in the velocity dispersion is closely related to the shear motion, which depends on  $\kappa/\Omega$  but not on  $\nu/\Omega$ , the parameter  $\nu/\Omega$  is fixed to 1.0. In the limit of  $\kappa/\Omega \rightarrow 2.0$ , shear motion vanishes so that orbital integration becomes difficult. The case with  $\kappa/\Omega \sim 1$  is well investigated by several authors (e.g. Ida 1990, Kokubo & Ida 1992), hence we are mainly concerned with the results with  $\kappa/\Omega = 1.58, 1.73$ , and  $1.87$ .

First we show the results for  $\kappa/\Omega = 1.87$ . In this case, we calculated  $P_{\text{heat}}$  and  $Q_{\text{heat}}$  for 392 sets of  $e$  and  $i$ . For each set of  $(e, i)$ , we integrated  $10^4 - 10^6$  orbits with different sets of  $(b, \tau, \omega)$ . In Figs. 3-a to 3-c, we show obtained  $p(e, i, b)$  (solid lines) and  $q(e, i, b)$  (dotted lines) as functions of  $b$ . In-

tegration of  $p$  and  $q$  with  $b$  yields  $P_{\text{heat}}$  and  $Q_{\text{heat}}$  (Eqs. (10)). In Figs. 3-a, b, and c,  $(e, i) = (0.19, 0.19)$ ,  $(1.23, 1.23)$ , and  $(10.1, 5.04)$ , respectively. Individual figures correspond to the results in the shear dominant region, the horseshoe dominant region, and the dispersion dominant region, which we define below. These figures suggest that only intermediate  $b$  contributes to the heating. The orbits with the intermediate  $b$  can closely approach each other. The orbits with smaller  $b$  turns back at distant  $y$  by the Coriolis force ('horseshoe orbits' (Brown 1911)), while those with larger  $b$  pass by at distant  $x$ . Ida (1990) and Kokubo & Ida (1992) showed that cumulative contribution ( $P_{\text{heat}}$  and  $Q_{\text{heat}}$ ) of distant encounters with large  $b$  is negligible even if it is integrated over  $b$  to infinity.

In the case of large  $e$ , the range of the strongly perturbed orbits in the  $b$ -space is extended by large amplitude of radial excursion,  $e\Omega/\kappa$ , as shown in Fig. 3. In the unperturbed orbits, the condition for orbit crossing is  $|b| < e\Omega/\kappa$  (Eq.(19)). Hence we usually calculate orbits in the range of  $0.6 \lesssim b \lesssim e\Omega/\kappa + 2.5$ . In the cases of Figs. 3-a, b, and c, we calculated  $3 \times 10^4$ ,  $7 \times 10^4$ , and  $4.3 \times 10^6$  orbits. The numbers of calculated orbits are large enough that the integrated values of  $P_{\text{heat}}(e, i)$  and  $Q_{\text{heat}}(e, i)$  change by less than 5-10 per cent by the choice of calculated sets of initial conditions.

In Fig. 4, we compile the calculated results for 392 sets of  $(e, i)$  with vectors. The angle between a vector and  $e$ -axis is determined by

$$\theta = \tan^{-1} \left( \frac{Q_{\text{heat}}/i^2}{P_{\text{heat}}/e^2} \right),$$

while the length of the vectors are defined as  $a \log[b(|P|/e^2 + |Q|/i^2 + 1)]$ , where  $a$  and  $b$  are constants chosen for the vectors to be easily seen (in Fig. 4,  $a = 0.2$  and  $b = 200$ ), and the factor 1 is introduced so that the length is always positive. These vectors show evolution trend of  $e$  and  $i$ . If a vector points to upper-right direction ( $\theta = 45^\circ$ ),  $e$  and  $i$  increase keeping  $i/e$  constant. Since

$$\frac{d(i/e)}{dt} = \frac{i}{2e} \left( \frac{1}{i^2} \frac{di^2}{dt} - \frac{1}{e^2} \frac{de^2}{dt} \right),$$

$i/e$  is kept constant when

$$\frac{1}{i^2} \frac{di^2}{dt} = \frac{1}{e^2} \frac{de^2}{dt}$$

or equivalently,

$$Q_{\text{heat}}/i^2 = P_{\text{heat}}/e^2.$$

The evolution of  $e$  and  $i$  is divided into two steps. The first evolution is relatively rapid evolution toward the equilibrium state of  $i/e$ , and the second one is the gradual increase in  $e^2 + i^2$  keeping  $i/e$  constant. Fig. 4 suggests that the first step is faster than the second one. In the case where  $e$  and  $i$  are sufficiently large, we can quantitatively show the time-scale of the first step is much shorter than that of the second one (Appendix A). As a result,  $e$  and  $i$  would evolve along the line where vectors gather. Since  $de^2/dt = CP_{\text{heat}}$  and  $di^2/dt = CQ_{\text{heat}}$ , where  $C$  is some constant, we can integrate typical trajectory of a particle on the  $e$ - $i$  plane using the data in Fig. 4 and their interpolation. The trajectory with initial condition  $(e, i) = (0.126, 0.126)$  is plotted as dashed line in Fig. 4. Since the trajectory reaches the

equilibrium state of  $i/e$  rapidly, it corresponds to a set of  $(e, i)$  in the 'equilibrium' state.

Fig. 4 shows three different regions according to the manner of the evolution of  $e$  and  $i$ , in particular, equilibrium ratio  $i/e$ : *shear dominant region* ( $e, i \lesssim 0.4$ ), *horseshoe dominant region* ( $0.4 \lesssim e, i \lesssim 2$ ), and *dispersion dominant region* ( $e, i \gtrsim 2$ ). In each region, the equilibrium ratio  $i/e$  is  $\ll 1$ ,  $\sim 1.1$ , and  $\sim 0.7$ , respectively, in the case where  $\kappa/\Omega = 1.87$ .

#### *shear dominant region*

In the shear dominant region, the vertical and horizontal epicycle amplitude are small and shear motion dominates. Since shear motion is horizontal and orbits are bent before the orbits come close to each other, gravitational scattering takes place two-dimensionally. Accordingly,  $i$  hardly changes as shown in Fig. 3-a. Dominant perturbation to  $e$  comes from orbits with  $b \sim 2$ . These orbits are distant 'horseshoe'-type encounters as shown in Fig. 5-a.

The orbital behaviour changes where the epicyclic oscillation velocity,  $(e^2 + i^2)^{1/2} \sim \sqrt{2}e$ , is comparable to the shear velocity, namely, where  $\alpha b/2 \sim \sqrt{2}e$  (see Eqs. (20)). Hence the boundary should be  $e \sim 0.35$ , which is consistent with Fig. 4.

#### *dispersion dominant region*

When  $e, i \gtrsim \alpha$ , approach velocity is dominated by the random velocity  $v = (e^2 + i^2)^{1/2} r_g \Omega$  rather than the shear velocity ( $\alpha b r_g \Omega/2$ ), and simultaneously, scattering occurs three dimensionally. Further, when the epicycle amplitude  $e r_g \Omega/\kappa$  is larger than the tidal radius  $r_t$ , where  $r_t$  is defined by

$$\begin{aligned} r_t &= \left( \frac{G(m_1 + m_2)}{\alpha \Omega^2} \right)^{\frac{1}{3}} \\ &= r_g \alpha^{-1/3}, \end{aligned} \quad (21)$$

that is, when  $e \gtrsim (\kappa/\Omega)\alpha^{-1/3}$ , orbits are not perturbed until the distance between bodies is much smaller than  $r_t$ , since scattering cross section is small according to high relative velocity. Fig. 5-c shows an example of orbital behaviour in this region. The orbit is hardly perturbed except when the distance is well smaller than  $r_t$ . In this case, impulse approximation adopted by IKM93 is valid. They adopted Rutherford scattering formula neglecting a disc potential, and assumed incident motion to the two-body Rutherford scattering is described by the unperturbed motion given by Eqs. (19) and (20). Actually, numerically obtained  $P_{\text{heat}}$ ,  $Q_{\text{heat}}$ , and  $e - i$  ratio in this region are in good agreement with those given by IKM93: in Fig. 3-c, dashed line denotes  $p(e, i, b)$  and  $q(e, i, b)$  calculated by IKM93, and the integrated quantities, i.e.,  $P_{\text{heat}}$  and  $Q_{\text{heat}}$  are in agreement with those obtained by IKM93 within accuracy of 10 per cent. In the region of small  $b$ , the analytical results deviate from the numerical ones, however, this deviation disappears when averaged over  $b$ . This is because some cancelation with regard to  $\tau$  or  $\omega$  for fixed  $b$  in the analytical calculation would be transferred to cancelation for slightly different  $b$  by weak distant perturbation in the numerical calculation.

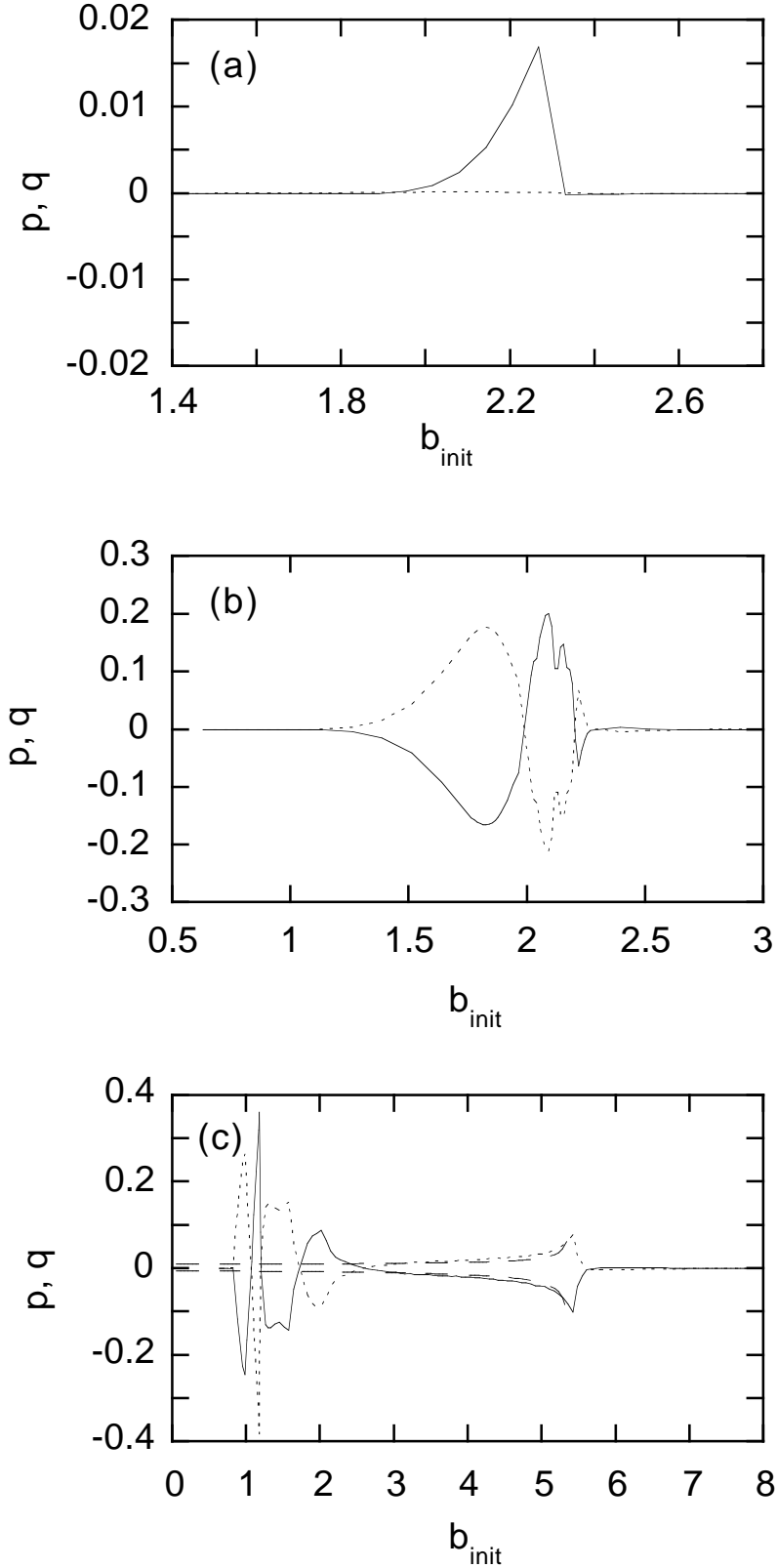


**Figure 3.** Dependence of  $p(e, i, b)$  (solid lines) and  $q(e, i, b)$  (dotted lines) on initial  $b$ . (a) Case with  $(e, i) = (0.19, 0.19)$ . The  $b$ -dependence is plotted every 0.05 ( $= \delta b$ ). To evaluate one point,  $50 \times 25$  orbits with different  $\tau$  and  $\omega$  are integrated. (b) Case with  $(e, i) = (1.23, 1.23)$ . In this case, we varied  $\delta b$  according to  $b$ -dependence of  $p$  or  $q$  (we took smaller  $\delta b$  where  $p$  or  $q$  rapidly changes):  $\delta b = 0.01$ -0.1. (c) Case with  $(e, i) = (10.1, 5.04)$ . As well as the case (b), we varied  $\delta b$  according to  $b$ -dependence of  $p$  or  $q$  so that  $\delta b = 0.01$ -0.2. For each  $b$ , we calculated  $100 \times 50$  -  $400 \times 200$  orbits with different  $\tau$  and  $\omega$ . We also plot IKM93's result (dashed lines).

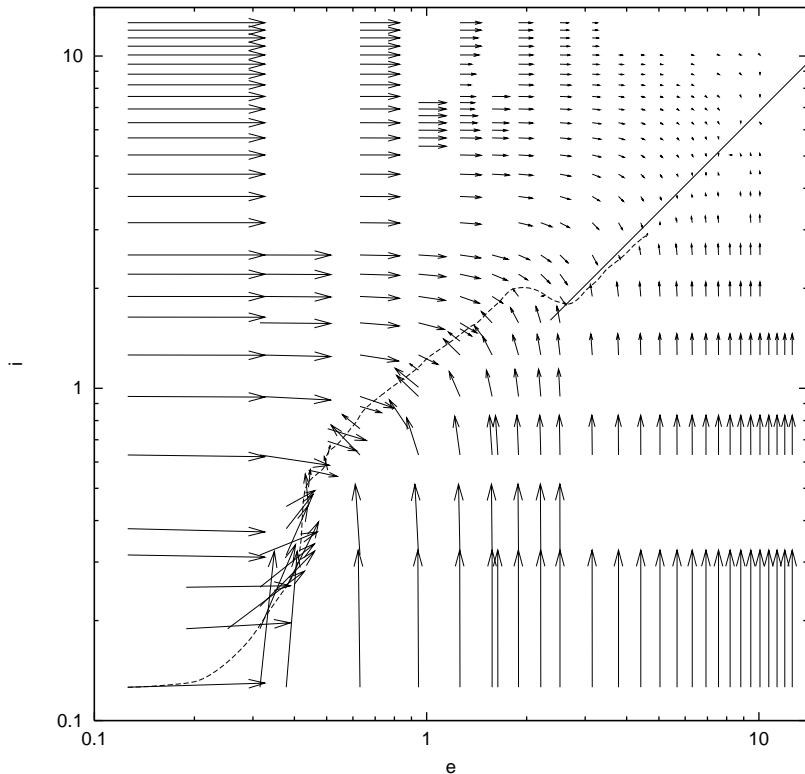


**Figure 4.** Directions and magnitude of the evolution of  $e$  and  $i$  on the  $e$ - $i$  plane in the case where  $\kappa/\Omega = 1.87$ . The angles of the vectors are given by  $\tan^{-1}(Q_{\text{heat}}e^2/P_{\text{heat}}i^2)$  and the length is  $\max(a, a \log[b(|P|/e^2 + |Q|/i^2 + 1)])$ , where  $a = 0.2$  and  $b = 200$ . Dashed line denotes the trajectory with initial condition  $(e, i) = (0.126, 0.126)$ . Solid line denotes the line  $i = 0.68e$  which is predicted by IKM93.

In Fig. 4, solid line denotes  $i/e = 0.68$  which is predicted by IKM93. This is also consistent with numerical results for  $e \gtrsim (\kappa/\Omega)\alpha^{-1/3} \simeq 2.4$ .

In the dispersion dominant region,  $i/e$  in the equilibrium state is smaller than unity. The origin of this anisotropic velocity dispersion is explained as follows (IKM93). In the dispersion dominant region, relative motion is approximated by unperturbed one as in Fig. 5-c, and close encounter always takes place when the particle is moving leftward (rightward) if  $b > 0$  ( $b < 0$ ). Hence at the moment of the closest approach, the horizontal component of the particle's incident velocity is always decelerated by the shear motion. On the other hand, the vertical motion is not affected by the shear and such a deceleration does not occur. At the moment of the closest approach, two-body scattering neglecting the tidal force can be applied, so that scattering tends to make (local) velocity isotropic, that is, equal energy is partitioned to each direction locally. Consequently, because of the deceleration of the horizontal motion at the closest approach, excessive energy is transferred to  $x$ - and  $y$ -directions compared to the  $z$ -direction. Hence in the dispersion dominant region, the equilibrium value of  $i/e$  is smaller than unity.

As shown in Fig. 3-c, heating is dominated almost equally by orbits with  $0.6 \lesssim b \lesssim e\Omega/\kappa$ . As described before, the upper limit  $e\Omega/\kappa$  comes from the crossing condition of an unperturbed orbit. Hence, in large  $e$  case, orbits with correspondingly large  $b$  necessarily contribute to the heating. In other words, encounters with large shear necessarily

contribute. This is the case even in the limit of the solid-body rotation. Thus IKM93 obtained  $i/e \sim 0.8 (< 1)$  even in the solid-body rotation case. As shown below, however, this anisotropic dispersion region practically disappears.

#### *horseshoe dominant region*

In the region with  $\alpha/\sqrt{2} \lesssim e \lesssim (\kappa/\Omega)\alpha^{-1/3}$ , approach velocity is dominated by random velocity as in the dispersion dominant region. However, orbital behaviour is quite different from that in the dispersion dominant region. In this region, relative velocity is not as high as that in the dispersion dominant region, so that relative motion is affected by distant perturbation similar to the shear dominant region. Figure 5-b shows an example of an orbit in this region. The orbit of guiding centre is gradually bent by Coriolis force until the orbit has  $b$  of different sign to turn back. Usually, such an orbit with  $e = i = 0$  is called 'horseshoe orbits'. Motion of guiding centre is similar to 'horseshoe orbits' even in the case of  $e, i \neq 0$ , since  $e$  and  $i$  are adiabatic invariants in distant region (Hénon & Petit 1986). In this paper, we use the name 'horseshoe orbits' even if  $e, i \neq 0$ .

As shown in Fig. 3-b, heating is dominated by orbits with  $0.6 \lesssim b \lesssim 2$  in this velocity region. When  $b \lesssim 2$ , the horseshoe orbits are common, because Coriolis force dominates shear motion. However, in contrast with shear-dominated case, larger epicycle amplitude enables the bod-

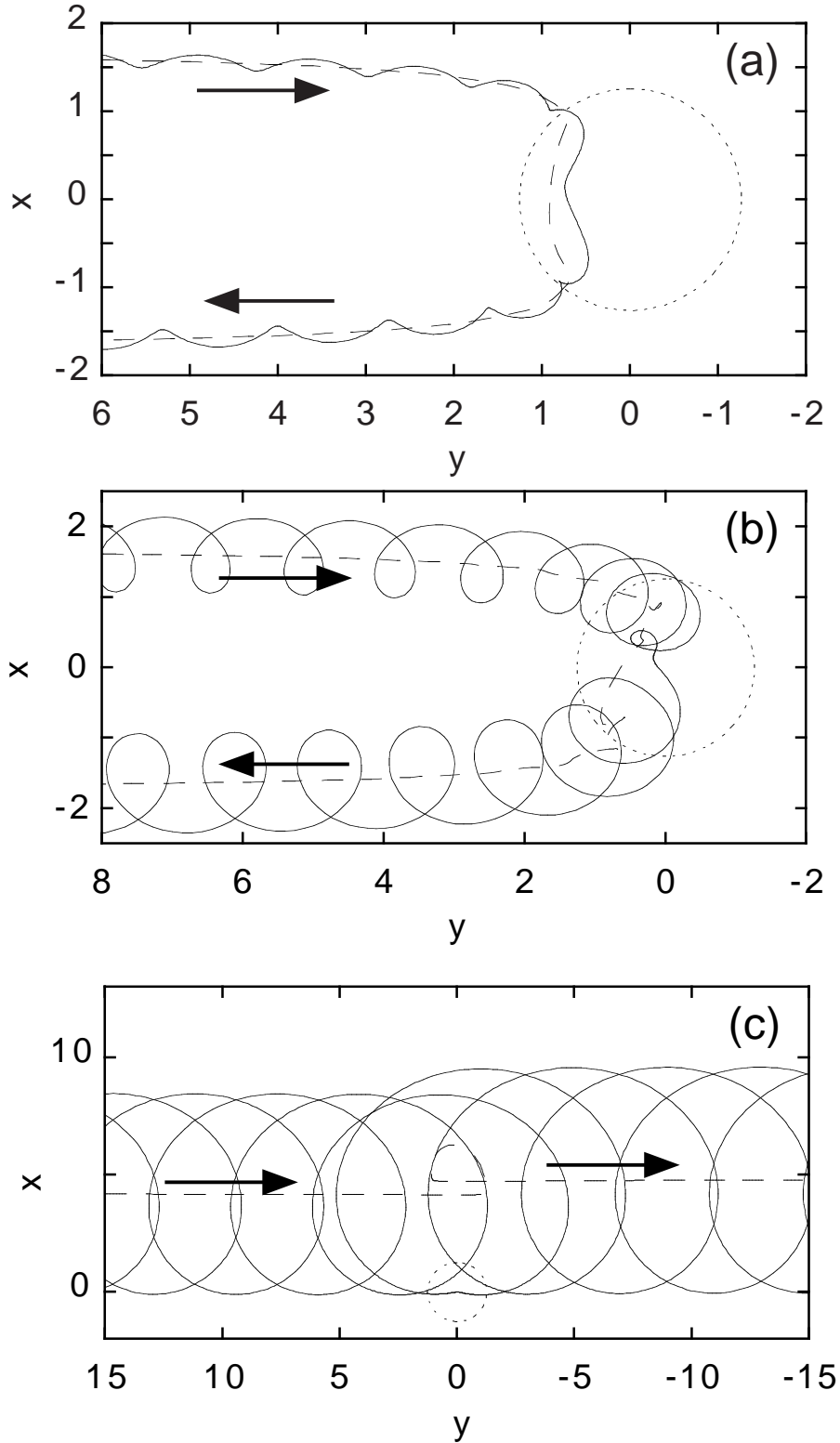


**Figure 5.** Examples of orbit in the shear dominant region (a), the horseshoe dominant region (b), and the dispersion dominant region (c) in the case where  $\kappa/\Omega = 1.87$ . The solid lines denote the orbit, the dashed lines the guiding-center motion, and the circle with dotted line represents the tidal sphere ( $r = r_t$ ). Arrows represents the directions of the guiding-center motion. In each figure, initial orbital elements are  $(e, i, b) = (0.19, 0.19, 2.14)$  in (a),  $(e, i, b) = (1.23, 1.23, 2.14)$  in (b), and  $(e, i, b) = (10.1, 5.04, 4.2)$  in (c) (we omitted the other orbital elements such as phase variables).



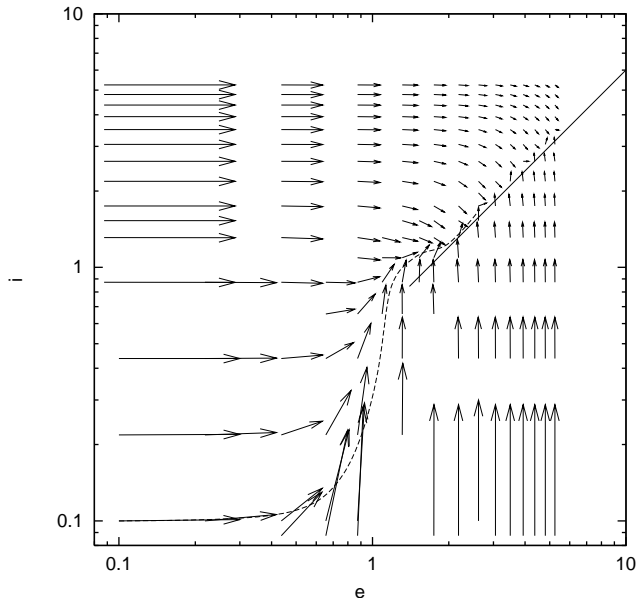


**Figure 6.** The same as Fig. 4 but  $\kappa/\Omega = 1.58$ . The solid line denotes  $i = 0.60e$  predicted by IKM93

ies to closely approach. In fact, close-encountering ‘horseshoe orbits’ as in Fig. 5-b contribute a lot to  $P_{\text{heat}}$  and  $Q_{\text{heat}}$ .

From the above orbital behaviour, the equilibrium ratio  $i/e \sim 1$  is realized as follows. On the contrary to the dispersion dominant case, a close encounter always takes place when the particle is moving in the same direction as the guiding-centre motion (see Fig. 5-b). Hence, the particle’s horizontal motion is locally accelerated at the close encounter. Consequently, the same argument as in the dispersion dominant region predicts that  $i/e$  should become larger than unity. However, because the motion of the guiding centre which is proportional to  $b$  is relatively slow, significant anisotropy does not appear. In the limit of the solid-body rotation, shear motion, and hence, the motion of the guiding centre slows down. Then  $i/e \simeq 1$  would be realized.

So far we have considered the case where  $\kappa/\Omega = 1.87$ . Our result in this case suggests that

$$\begin{cases} \text{the shear dominant region:} & e \lesssim \alpha/\sqrt{2}, \\ \text{the horseshoe dominant region:} & \alpha/\sqrt{2} \lesssim e \lesssim (\kappa/\Omega)\alpha^{-1/3}, \\ \text{the dispersion dominant region:} & (\kappa/\Omega)\alpha^{-1/3} \lesssim e, \end{cases} \quad (22)$$

where  $\alpha = 4 - \kappa^2/\Omega^2$ . To confirm the relation (22), we also calculated the cases with  $\kappa/\Omega = 1.58$  and  $1.73$  (Fig. 6 and 7). For  $\kappa/\Omega = 1.58$ , we calculated 208 sets of  $(e, i)$ , and for  $\kappa/\Omega = 1.73$ , 218 sets of  $(e, i)$  are calculated. In each case, as in Fig. 4, we integrated typical trajectory of a particle on the  $e$ - $i$  plane (dashed lines). The solid lines are also added as the result of IKM93. Expected boundaries of the regions in the individual cases are shown in Table 1. Figs. 4, 6 and 7 agree with Table 1.

The horseshoe dominant region shrinks as  $\kappa/\Omega$  decreases. The horseshoe dominant region would vanish for

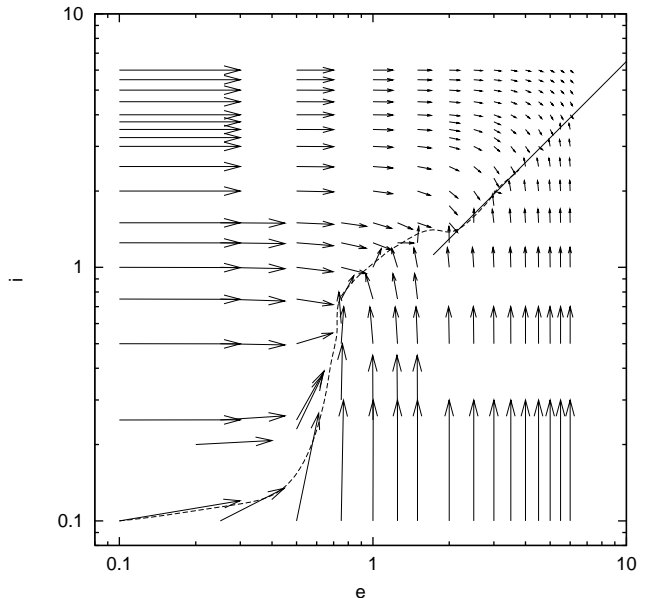


**Figure 7.** The same as Fig. 4 but  $\kappa/\Omega = 1.73$ . The solid line denotes  $i = 0.65e$  predicted by IKM93

**Table 1.** Boundaries among three regions.

$\kappa/\Omega$	$\alpha/\sqrt{2}$	$(\kappa/\Omega)\alpha^{-1/3}$
1.58	1.0	1.4
1.73	0.7	1.7
1.87	0.35	2.4

$\alpha/\sqrt{2} \gtrsim (\kappa/\Omega)\alpha^{-1/3}$  (equivalently,  $\kappa/\Omega \lesssim 1.5$ ). However, it should be noted that the ‘horseshoe’-type close encounters still occur even if  $\kappa/\Omega \lesssim 1.5$ . We found when  $\kappa/\Omega = 1.30$ , this effect makes the equilibrium ratio slightly larger than that predicted by IKM93 for  $e \sim 2$ -3.

Since Ida (1990) and Kokubo & Ida (1992) only studied the cases with  $\kappa/\Omega = 1.0$  and  $\kappa/\Omega = 1.39$ , respectively, they did not find the horseshoe dominant region. On the other hand, the horseshoe dominant region expands and dominates other two regions as  $\kappa/\Omega$  approaches 2 ( $\alpha \rightarrow 0$ ). Therefore, in the limit  $\kappa/\Omega \rightarrow 2$ , the region in which  $i/e \sim 1$  is realized covers all over velocity space except for  $e \rightarrow \infty$ . In the limit with  $e \rightarrow \infty$ , IKM93’s analysis would still be correct. The IKM93’s analysis, which well accounts for  $i/e$  in low  $\kappa/\Omega$  case, is also valid in high  $\kappa/\Omega$  case if  $e$  is sufficiently large, but the isotropic velocity region actually dominates in that case. Thus the contradiction stated in the introduction is solved.

### 2.3 The Effect of Averaging on the Rayleigh Distribution Function

Here we present the heating rates with the Rayleigh distribution. This is necessary not only because the realistic velocity distribution must be considered, but also because we compare the results to those of  $N$ -body simulations in the next section.

Our numerical calculation of the heating rates  $P_{\text{heat}}$  and

$Q_{\text{heat}}$  is restricted within  $e, i \lesssim 12$ . By comparing numerically obtained  $P_{\text{heat}}$  and  $Q_{\text{heat}}$  to those of IKM93, as stated in the last subsection, we find both are in agreement within accuracy of 10 per cent where  $e, i \gtrsim 7$  for  $\kappa/\Omega = 1.87$ . Accordingly, in the region with  $e \gtrsim 12$  or  $i \gtrsim 12$ , we use the analytical results of IKM93 in this case. In Fig. 8, we show the evolution diagram obtained from  $\langle P_{\text{heat}} \rangle$  and  $\langle Q_{\text{heat}} \rangle$  in the case of  $\kappa/\Omega = 1.87$ . The vectors drawn as a function of the root mean squares,  $\langle e_*^2 \rangle^{1/2}$  and  $\langle i_*^2 \rangle^{1/2}$  in the same manner as in Fig. 4 (here,  $a = 0.2, b = 1000$ ). Here, we use  $\langle e_*^2 \rangle^{1/2}$  and  $\langle i_*^2 \rangle^{1/2}$  as normalized velocity dispersion of particles and distinguish them from those of relative motion,  $\langle e^2 \rangle^{1/2}$  and  $\langle i^2 \rangle^{1/2}$ . Note that  $\langle e_*^2 \rangle^{1/2}$  ( $\langle i_*^2 \rangle^{1/2}$ ) and  $\langle e^2 \rangle^{1/2}$  ( $\langle i^2 \rangle^{1/2}$ ) are related by Eqs. (16). When mass of test particles 1 is much smaller than that of field particles 2,  $\langle e_*^2 \rangle^{1/2} = \langle e^2 \rangle^{1/2}$  and  $\langle i_*^2 \rangle^{1/2} = \langle i^2 \rangle^{1/2}$  owing to energy equipartition. On the other hand, in the system of identical mass,  $\langle e_*^2 \rangle^{1/2} = \langle e^2 \rangle^{1/2}/\sqrt{2}$  and  $\langle i_*^2 \rangle^{1/2} = \langle i^2 \rangle^{1/2}/\sqrt{2}$ . Hereafter we consider the system of identical mass in accordance with  $N$ -body simulations in the next section. Hence it should be noted that  $e_*$  is smaller than  $e$  by a factor  $\sqrt{2}$ . In this figure, we also plotted the typical trajectory in the same way as Fig. 4. Although averaging smoothes the boundaries of the three regions observed in Fig. 4, the behaviour of the equilibrium ratio of the velocity dispersion is basically the same as Fig. 4: In very small velocity case,  $\langle e_*^2 \rangle^{1/2} \gg \langle i_*^2 \rangle^{1/2}$ , in intermediate velocity case ( $\langle e_*^2 \rangle^{1/2}$  and  $\langle i_*^2 \rangle^{1/2}$  are of order unity), the equilibrium value is almost unity, and in larger velocity case the equilibrium value is less than unity and seems to approach the value which predicted by IKM93 (for example, in the equilibrium state,  $\langle i_*^2 \rangle^{1/2}/\langle e_*^2 \rangle^{1/2} \simeq 1.0$  for  $\langle i_*^2 \rangle^{1/2} = 2.0$ ,  $\langle i_*^2 \rangle^{1/2}/\langle e_*^2 \rangle^{1/2} \simeq 0.95$  for  $\langle i_*^2 \rangle^{1/2} = 4.0$ , and  $\langle i_*^2 \rangle^{1/2}/\langle e_*^2 \rangle^{1/2} \simeq 0.86$  for  $\langle i_*^2 \rangle^{1/2} = 9.0$ ). It should be noted that the obtained equilibrium ratio seems to approach IKM93's much more moderately than the case of Fig. 4: In the case where the averaging is not done, our results (the equilibrium ratio) almost coincide with IKM93's for  $e \gtrsim 2$ , while with the averaging, our results do not coincide with IKM93's even when  $\langle e_*^2 \rangle^{1/2}, \langle i_*^2 \rangle^{1/2} \sim 10$ . In other words, the horseshoe dominant region influences even if  $\langle e_*^2 \rangle^{1/2}$  and  $\langle i_*^2 \rangle^{1/2}$  are much larger than unity as a result of the averaging on the velocity distribution. Actually, we found the influence of the horseshoe dominant region remains as long as  $\langle i_*^2 \rangle^{1/2} \lesssim 30$  in the case of  $\kappa/\Omega = 1.87$  and  $\langle i_*^2 \rangle^{1/2} \lesssim 20$  for  $\kappa/\Omega = 1.58$ . On the other hand, in the case of Kepler rotation, where there is no horseshoe dominant region, we found that our numerical results coincide with IKM93's for  $\langle i_*^2 \rangle^{1/2} \gtrsim 2$ .

### 3 N-BODY SIMULATIONS OF THE DISC HEATING

#### 3.1 Basic equations

In section 2, we studied disc heating through statistical compilation of independent two-body scatterings. In this section, to check the results in section 2, we perform direct  $N$ -body simulations of particles in axisymmetric disc potentials. We consider  $N$  self-gravitating particles revolving in a disc potential. Then the motion of each particle is described as

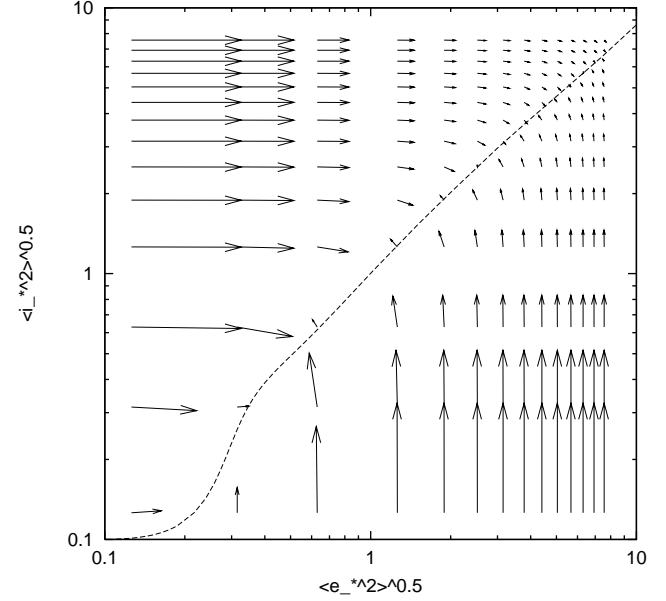


**Figure 8.** Direction of the evolution of  $\langle e_*^2 \rangle^{1/2}$  and  $\langle i_*^2 \rangle^{1/2}$  plotted on the  $\langle e_*^2 \rangle^{1/2} - \langle i_*^2 \rangle^{1/2}$  plane in the case of  $\kappa/\Omega = 1.87$ . The angle and length of each vector is determined in the same way as Fig. 4, but constants  $a = 0.2$  and  $b = 1000$ . Similar to Figs. 4, 6, and 7, we plot the typical trajectory as the dashed line.

$$\frac{d\mathbf{v}_j}{dt} = \sum_{i \neq j}^N Gm_j \frac{\mathbf{x}_i - \mathbf{x}_j}{|\mathbf{x}_i - \mathbf{x}_j|^3} + \mathbf{F}_j \quad (j = 1, \dots, N), \quad (23)$$

where the subscript  $j$  indicates particle's index,  $\mathbf{v}_j$ ,  $\mathbf{x}_j$ , and  $m_j$  are the velocity vector, the position vector, and the mass of the particle  $j$ . The last term on the right hand side,  $\mathbf{F}_j$ , is external force resulted from the disc potential. We consider the radial and vertical excursion of each particle are sufficiently small compared to its orbital radius in accordance with the study in the last section. In this case, the external force field  $\mathbf{F}_j$  is expressed by two parameters of the disc potential,  $\alpha$  and  $\nu/\Omega$ , as

$$\begin{cases} F_{xj} = -a\Omega^2 \left( \frac{x_j}{a} \right) \left[ \frac{R_j^2}{a^2} + \left( \frac{\nu}{\Omega} \right)^2 \frac{z_j^2}{a^2} \right]^{-\frac{\alpha}{2}}, \\ F_{yj} = -a\Omega^2 \left( \frac{y_j}{a} \right) \left[ \frac{R_j^2}{a^2} + \left( \frac{\nu}{\Omega} \right)^2 \frac{z_j^2}{a^2} \right]^{-\frac{\alpha}{2}}, \\ F_{zj} = -a\Omega^2 \left[ \left( \frac{\nu}{\Omega} \right)^2 \frac{z_j}{a} \right] \left[ \frac{R_j^2}{a^2} + \left( \frac{\nu}{\Omega} \right)^2 \frac{z_j^2}{a^2} \right]^{-\frac{\alpha}{2}}, \end{cases} \quad (24)$$

where Cartesian coordinates  $(x, y, z)$  is centred at the bottom of the disc potential,  $R$  is the radial component of cylindrical coordinates given by  $R = (x^2 + y^2)^{1/2}$ .

We integrate Eqs. (23) by using the fourth-order Hermite scheme with the individual and hierarchical timestep (Makino 1991). The most expensive part of the Hermite scheme is the calculation of the force and its time-derivative whose cost increases in proportion to  $N^2$  because we calculate the direct sum of all pairs. To reduce the computational time of this part, we employed a special purpose hardware, HARP-2 (Makino, Kokubo & Taiji 1993) and GRAPE-4 (Makino, Taiji, Ebisuzaki & Sugimoto 1997).

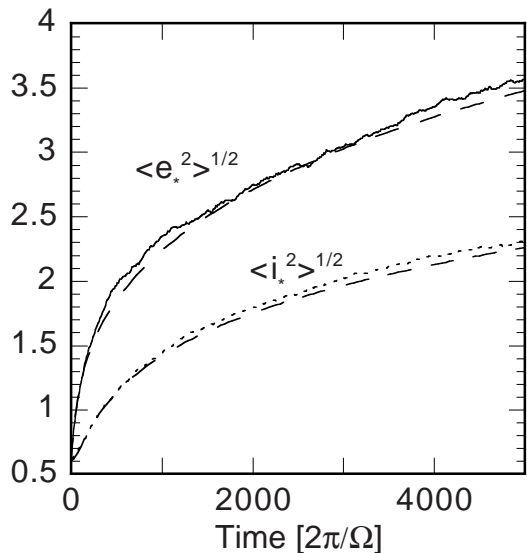


**Figure 9.** Time evolutions of  $\langle e_*^2 \rangle^{1/2}$  (solid line) and  $\langle i_*^2 \rangle^{1/2}$  (dotted line) in the case of run 8. Time is scaled by the rotation period at  $R = a$  ( $2\pi/\Omega(a)$ ). The dashed lines denote time evolutions of the normalized velocity dispersion predicted by  $d\langle e_*^2 \rangle/dt$  and  $d\langle i_*^2 \rangle/dt$  given by Eqs. (13) and the two-body results in section 2.

### 3.2 Initial conditions of the swarm of particles

We mainly investigated the  $\kappa/\Omega$  dependence of the equilibrium ratio of velocity dispersion. The parameter  $\nu/\Omega$  is fixed to be unity in most cases, since IKM93 suggested that it does not affect the equilibrium ratio (we also did some  $N$ -body simulations with  $\nu/\Omega \neq 1$  and found that the ratio is the same as in the case with  $\nu/\Omega = 1$ ). We did 27  $N$ -body simulations with nine different values of  $\kappa/\Omega$ . For each value of  $\kappa/\Omega$ , we did several runs starting with different initial conditions.

In Table 2, we summarize the initial conditions. We distribute 1000 particles with identical mass randomly in the region  $a - \Delta a/2 < a < a + \Delta a/2$ . In most cases, the particle masses are  $m = 3 \times 10^{-9} M_g$  where  $M_g$  is effective mass of the center defined by  $GM_g/a^2 = \Omega^2 a$ . As suggested by the argument in section 2, the results would be independent of particle masses, if the results are scaled by  $r_g$ . We took  $\Delta a \ll a$  to make simulation radially local, however, we took  $\Delta a$  sufficiently larger than  $r_t$  (characteristic size of a particle's potential well) and epicycle amplitude for the edge effects to be negligible. We used enough number ( $N = 1000$ ) of bodies that the bodies can closely approach each other. Initially, we set the same  $e_*$  and  $i_*$  ( $e_{*0}, i_{*0}$ ) for all particles, however, the velocity distribution converges to the Rayleigh distribution given by Eq. (17) in shorter time interval compared to the characteristic time-scale of the evolution of the velocity dispersion (i.e., two-body relaxation time  $T_{2B}$ ).

### 3.3 Results of the $N$ -body simulations

First we show the detailed results in two characteristic cases with  $\kappa/\Omega = 1.30$  and  $\kappa/\Omega = 1.87$ . As stated before, orbital properties change near  $\kappa/\Omega \sim 1.5$ .

In Fig. 9, we show the time evolutions of  $\langle e_*^2 \rangle^{1/2}$  (solid

**Table 2.** Initial parameters in  $N$ -body simulations.

run	$\kappa/\Omega$	$\nu/\Omega$	$e_{*0}$	$i_{*0}$	$\Delta a/a$
1	1.00	1.00	0.6	0.6	0.29
2	1.00	1.00	0.6	1.2	0.27
3	1.00	1.00	1.1	0.3	0.27
4	1.10	1.00	0.2	0.2	0.13
5	1.10	1.00	0.2	0.4	0.13
6	1.20	1.00	0.5	0.5	0.27
7	1.20	1.00	0.5	0.8	0.27
8	1.30	1.00	0.6	0.6	0.33
9	1.30	1.00	0.6	1.2	0.27
10	1.30	1.00	1.2	0.3	0.27
11	1.30	2.00	0.6	0.6	0.29
12	1.30	4.00	0.6	0.6	0.29
13	1.58	1.00	2.0	1.0	0.27
14	1.58	1.00	1.0	2.0	0.27
15	1.73	1.00	0.1	0.1	0.27
16	1.73	1.00	0.4	0.2	0.27
17	1.80	1.00	1.0	0.5	0.27
18	1.80	1.00	2.0	1.0	0.27
19	1.80	1.00	1.0	2.0	0.27
20	1.87	1.00	1.1	0.6	0.27
21	1.87	1.00	2.0	1.0	0.27
22	1.87	1.00	1.0	2.0	0.27
23	1.87	2.00	1.0	2.0	0.27
24	1.87	4.00	1.0	2.0	0.27
25	1.95	1.00	1.0	0.5	0.27
26	1.95	1.00	2.0	1.0	0.27
27	1.95	1.00	1.0	2.0	0.27

line) and  $\langle i_*^2 \rangle^{1/2}$  (dotted line) of run 8 ( $\kappa/\Omega = 1.30$ ). The parameter  $\kappa/\Omega = 1.30$  corresponds to the galactic potential in the solar neighbourhood. In the figure, time is scaled by the rotation period at  $a$ , namely,  $2\pi/\Omega(a)$ . Although both  $\langle e_*^2 \rangle^{1/2}$  and  $\langle i_*^2 \rangle^{1/2}$  keep growing, the ratio of  $\langle i_*^2 \rangle^{1/2}$  to  $\langle e_*^2 \rangle^{1/2}$  seems to be constant in the later stage. The ratio  $\langle i_*^2 \rangle^{1/2} / \langle e_*^2 \rangle^{1/2}$  is plotted as a function of  $\langle e_*^2 + i_*^2 \rangle^{1/2}$  in Fig. 10, which is equivalently, time evolution of  $\langle i_*^2 \rangle^{1/2} / \langle e_*^2 \rangle^{1/2}$ . We also plot the results with different sets of ( $e_{*0}, i_{*0}$ ) for the same  $\kappa/\Omega$  (run 9 and 10). The ratio of the velocity dispersions settles to a certain constant ( $\sim 0.6$ ) value independent of initial values of  $e_*$  and  $i_*$  after  $\langle e_*^2 + i_*^2 \rangle^{1/2}$  exceeds about 3. The equilibrium ratio gradually increases as  $\langle e_*^2 + i_*^2 \rangle^{1/2}$ , which is consistent with the analytical argument in IKM93 that the equilibrium ratio has a weak dependence on  $\langle e_*^2 + i_*^2 \rangle^{1/2}$ .

The equilibrium ratio  $\langle i_*^2 \rangle^{1/2} / \langle e_*^2 \rangle^{1/2} \sim 0.6$  is consistent with the observational value given by Wielen (1977) and Chen et al. (1996), statistical compilation of two-body encounters by Kokubo & Ida (1992), and  $N$ -body simulation by Villumsen (1985).

The time evolution of  $\langle e_*^2 \rangle^{1/2}$  and  $\langle i_*^2 \rangle^{1/2}$  in the case of  $\kappa/\Omega = 1.87$  (run 22) is shown in Fig. 11. Solid and dotted lines express  $\langle e_*^2 \rangle^{1/2}$  and  $\langle i_*^2 \rangle^{1/2}$ . The increase in  $\langle e_*^2 \rangle^{1/2}$  is almost compensated by decrease in  $\langle i_*^2 \rangle^{1/2}$ . The system evolve to the state of the equilibrium ratio, without increase in  $\langle e_*^2 + i_*^2 \rangle^{1/2}$ , which is in contrast to the case

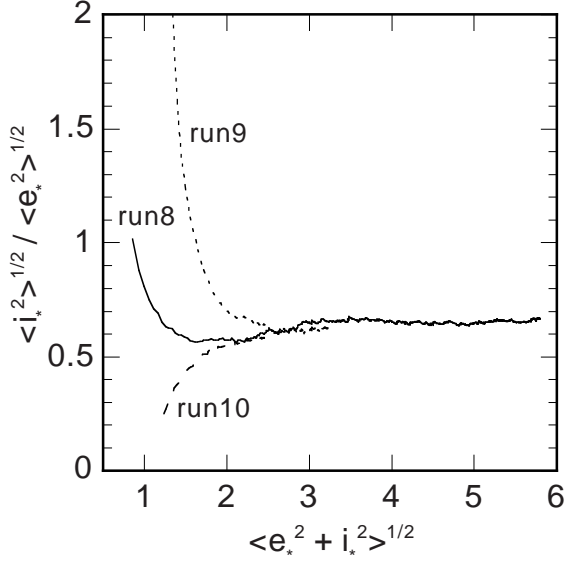


**Figure 10.** The evolution of ratio  $\langle i_*^2 \rangle^{1/2} / \langle e_*^2 \rangle^{1/2}$  against  $\langle e_*^2 + i_*^2 \rangle^{1/2}$  in the cases of run 8, 9, and 10 (the same initial parameters but different sets of initial  $e_{*0}$  and  $i_{*0}$ ). This is equivalent to the time evolution, since  $\langle e_*^2 + i_*^2 \rangle^{1/2}$  monotonically increases as time evolves.

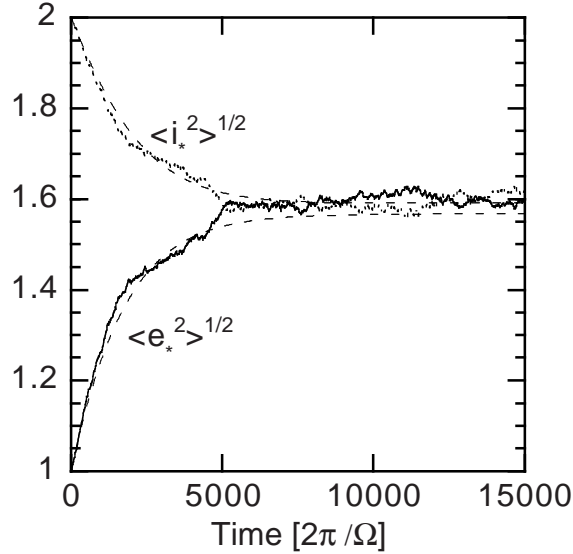


**Figure 11.** Time evolutions of  $\langle e_*^2 \rangle^{1/2}$  (solid line) and  $\langle i_*^2 \rangle^{1/2}$  (dotted line) in the case of run 22. The dashed lines denote time evolutions of the normalized velocity dispersion predicted by the two-body results in section 2.

of  $\kappa/\Omega = 1.30$ . Actually, the normalized random velocity  $\langle e_*^2 + i_*^2 \rangle^{1/2}$  only increases about 1 per cent throughout the simulation. This is consistent with the argument given in section 2 and appendix A ( $T_{\text{ratio}} \ll T_{\text{random}}$ ). In the potential with  $\kappa/\Omega = 1.87$ , orbital motion is close to solid-body rotation. Since disc heating is caused by transformation from shear motion to random motion, the disc heating is weak in the potential with  $\kappa/\Omega = 1.87$ . Gravitational interactions mostly result in redistribution of random energy.

In Fig. 12, we show the evolution of  $\langle i_*^2 \rangle^{1/2} / \langle e_*^2 \rangle^{1/2}$  with

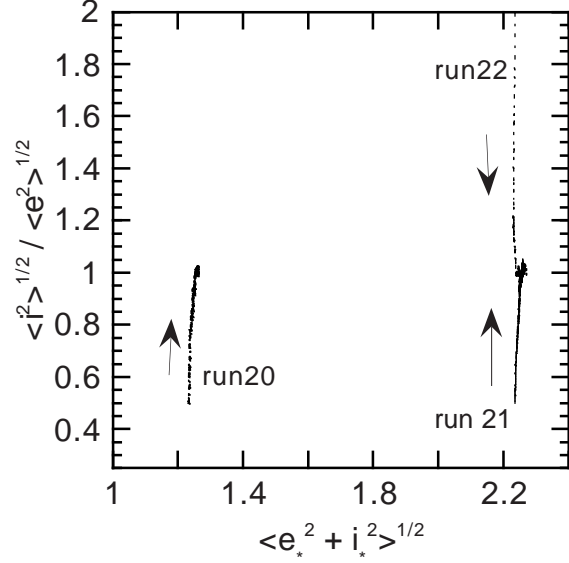


**Figure 12.** The evolution of ratio  $\langle i_*^2 \rangle^{1/2} / \langle e_*^2 \rangle^{1/2}$  against  $\langle e_*^2 + i_*^2 \rangle^{1/2}$  in the cases of run 20, 21, and 22.

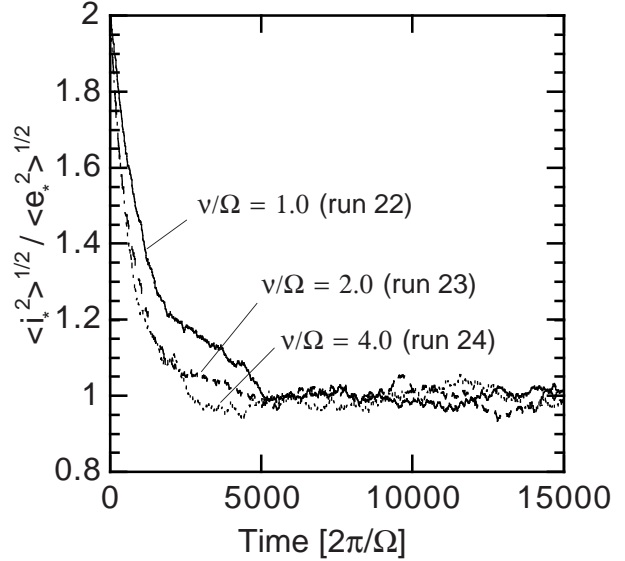


**Figure 13.** The time evolution of ratio  $\langle i_*^2 \rangle^{1/2} / \langle e_*^2 \rangle^{1/2}$  with various  $\nu/\Omega$ . Solid line corresponds to the results of run 22 ( $\nu/\Omega = 1.0$ ). Dashed and dotted lines for run 23 ( $\nu/\Omega = 2.0$ ) and run 24 ( $\nu/\Omega = 4.0$ ).

different values of  $\langle e_*^2 + i_*^2 \rangle^{1/2}$  (run 20, 21 and 22). This figure shows the equilibrium ratio settles to nearly unity independent of the initial conditions, as long as  $\langle e_*^2 \rangle^{1/2}$  and  $\langle i_*^2 \rangle^{1/2}$  are of order unity.

We found that the distributions of the  $e_*$  and  $i_*$  evolve from the initial  $\delta$ -function type function to the Rayleigh distribution in a time interval about  $< 0.1T_{2B}$  in both cases. Hence the assumption in Eq.(17) is valid.

In Figs. 9 and 11, we also plotted the evolution of the normalized velocity dispersion calculated from  $d\langle e_*^2 \rangle / dt$  and  $d\langle i_*^2 \rangle / dt$  obtained in section 2 (Eqs. (13)) as dashed lines.

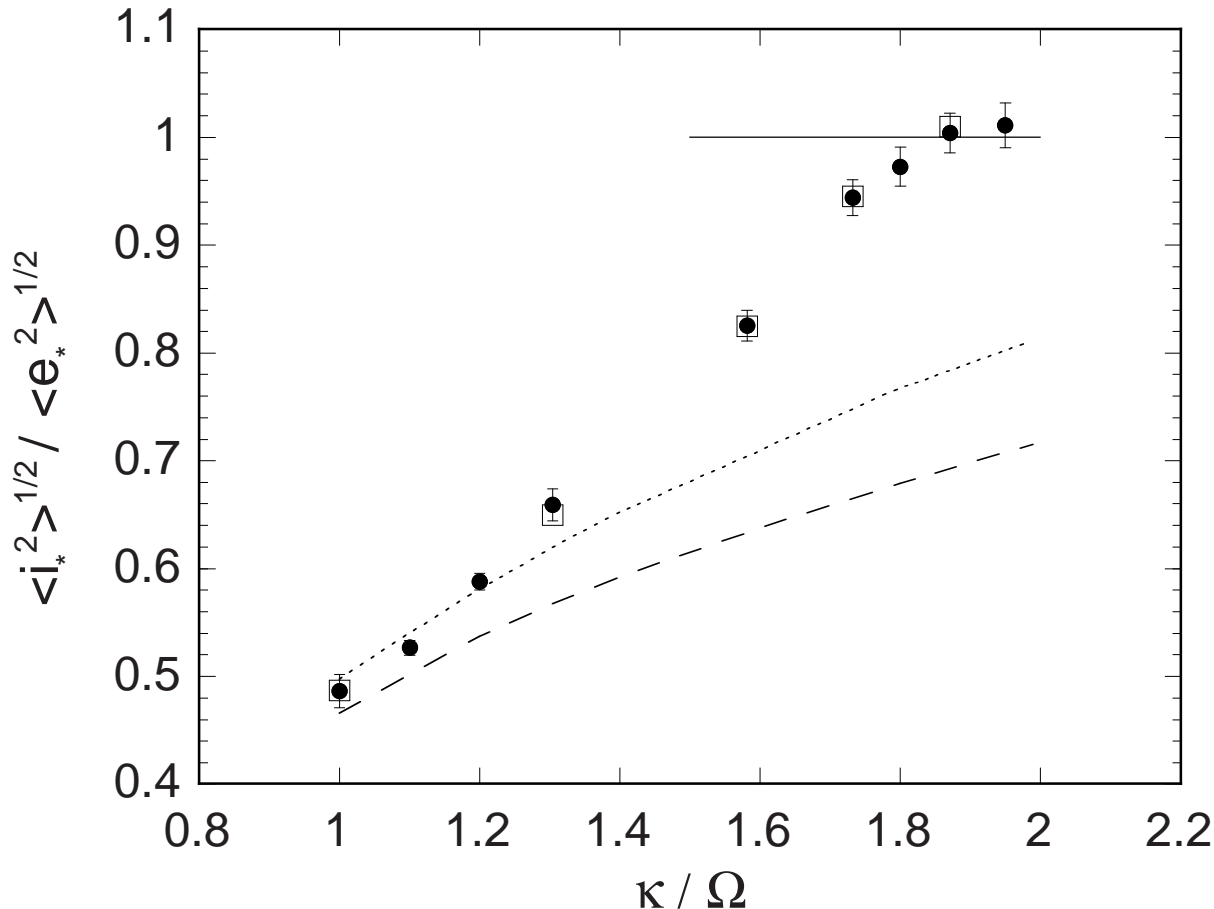


**Figure 14.** Equilibrium value of  $\langle i_*^2 \rangle^{1/2} / \langle e_*^2 \rangle^{1/2}$  as a function of  $\kappa / \Omega$ . Points with error bars are the results of the 27  $N$ -body simulations. Initial conditions of these simulations are presented in Table 2. Solid line corresponds to the isotropic state, i.e.,  $\langle i_*^2 \rangle^{1/2} / \langle e_*^2 \rangle^{1/2} = 1.0$ , which is realized in the horseshoe dominant region. Dashed and dotted curves denote the results of IKM93 in the cases where  $\langle i_*^2 \rangle^{1/2} = 1.5$  and  $\langle i_*^2 \rangle^{1/2} = 5.0$ , respectively. Open squares are the equilibrium ratio obtained by the two-body results in section 2 at the mean velocity corresponding to the  $N$ -body results.

In both cases, the predicted results are in good agreement with the results of  $N$ -body simulations.

In addition to the runs with  $\nu / \Omega = 1.0$ , we also did 4 simulations with  $\nu / \Omega = 2.0$  and 4.0 (run 11, 12, 23, and 24). In the solar neighbourhood,  $\nu / \Omega \simeq 4$  (Binney & Tremaine 1987). In these simulations, the other initial conditions are the same as run 8 for run 11 and 12, and the same as run 22 for run 23 and 24. The time evolution of  $\langle i_*^2 \rangle^{1/2} / \langle e_*^2 \rangle^{1/2}$  in the case of  $\kappa / \Omega = 1.87$  is shown in Fig. 13. The solid line denotes the result of run 22 ( $\nu / \Omega = 1.0$ ), the dashed line is that for run 23 ( $\nu / \Omega = 2.0$ ), and the dotted line for run 24 ( $\nu / \Omega = 4.0$ ). The variation of  $\nu / \Omega$  does not affect the equilibrium ratio as expected, though the larger  $\nu / \Omega$  results in the faster relaxation to the equilibrium state (This is because the larger  $\nu / \Omega$  leads to smaller disc scale height and therefore leads to more frequent scatterings among particles: see Eqs. (3)). These results are the cases also for  $\kappa / \Omega = 1.30$ .

We also carried out  $N$ -body simulations in the cases of  $\kappa / \Omega = 1.0, 1.1, 1.2, 1.73$ , and 1.95, as summarized in Table 2. In Fig. 14, we plot the equilibrium value of  $\langle i_*^2 \rangle^{1/2} / \langle e_*^2 \rangle^{1/2}$  obtained by the  $N$ -body simulations with filled circles where error bars indicate standard deviation in time evolution. In the shear dominant region, we found timescale for heating

(i.e.  $T_{2B}$ ) is comparable to or shorter than that for change of the ratio. Thus in the shear dominant region, there is no ‘equilibrium’ ratio. Accordingly, we are interested in the ratio in the dispersion dominant and the horseshoe dominant regions not in the shear dominant region. Since we cannot calculate the region with very large  $\langle e_*^2 \rangle^{1/2}$  and  $\langle i_*^2 \rangle^{1/2}$  for cpu limit, we only plot the results in the horseshoe dominant region in the cases of  $\kappa / \Omega \gtrsim 1.60$ . In the cases of  $\kappa / \Omega \lesssim 1.30$ , we plot the ratio in the dispersion dominant region, since there is no horseshoe dominant region.

Together with the  $N$ -body results, the line  $\langle i_*^2 \rangle^{1/2} / \langle e_*^2 \rangle^{1/2} = 1$  (the solid line) and the analytical lines in the dispersion dominant region by IKM93 are plotted. The dashed and dotted lines are IKM93’s results with  $\langle i_*^2 \rangle^{1/2} = 1.5$  and 5.0. In the plotted  $N$ -body results,  $\langle i_*^2 \rangle^{1/2} \simeq 1.5$ –5 except run 15, 18, and 21.

For  $\kappa / \Omega \sim 1.0$ –1.2, the  $N$ -body results almost agree with the analytical line. For  $\kappa / \Omega \gtrsim 1.87$ , the  $N$ -body results show isotropy ( $\langle i_*^2 \rangle^{1/2} / \langle e_*^2 \rangle^{1/2} \simeq 1$ ), which is expected in the horseshoe dominant region. However, for  $1.6 \lesssim \kappa / \Omega \lesssim 1.8$ , the  $N$ -body results are between the lines of IKM93 and the isotropy. As shown in section 2, the horseshoe dominant region is in limited velocity space in the case of relatively

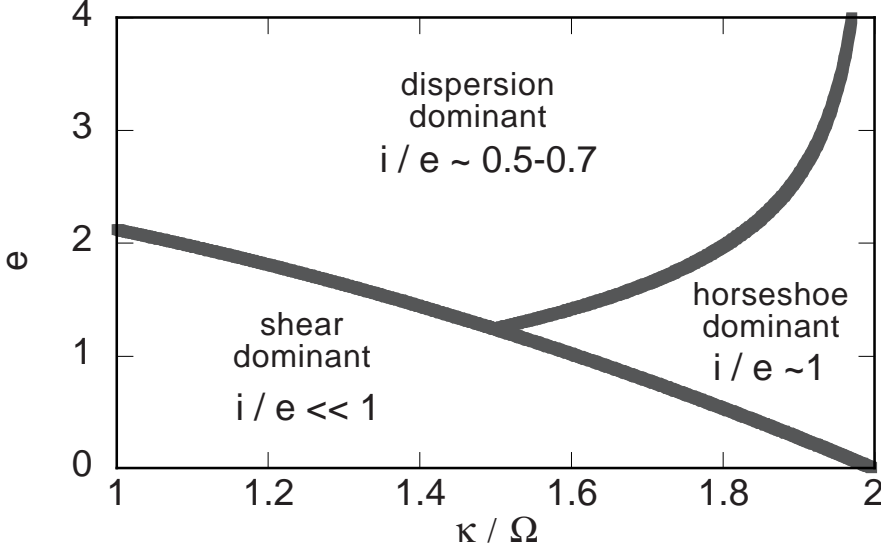


**Figure 15.** Boundaries among three regions obtained from the relation (25) and corresponding equilibrium ratios.

small  $\kappa/\Omega$ . Since the velocity distribution (Rayleigh distribution) includes “dispersion-dominant” encounters more or less, its effect decreases the  $\langle i_*^2 \rangle^{1/2} / \langle e_*^2 \rangle^{1/2}$  from 1. On the other hand, the contamination of ‘horseshoe’-type encounter would make  $\langle i_*^2 \rangle^{1/2} / \langle e_*^2 \rangle^{1/2}$  slightly larger than IKM93’s result as suggested in section 2. To confirm this interpretation, in Fig. 14 we also plot the results (squares) of section 2 with Rayleigh distribution at the mean velocity corresponding to the  $N$ -body results. They are consistent with the  $N$ -body results. It is expected that numerical results would be consistent with IKM93’s in sufficiently high mean velocity cases, because the effect of the horseshoe dominant region diminishes then. In section 2, however, we suggested influence of the horseshoe dominant region remains when  $\langle i_*^2 \rangle^{1/2} < 20$ -30 in the case where  $\kappa/\Omega = 1.58$ -1.87, as a result of the averaging effect. Unfortunately, because of numerical difficulty we cannot directly examine such a high velocity region with neither  $N$ -body simulation nor the method in section 2.  $N$ -body simulation with very high random velocity needs considerable cpu time since two-body relaxation time is proportional to the forth power of the random velocity in a disc system (Appendix A). The method in section 2 is difficult to apply since scattering cross-section becomes very small so that we cannot obtain reliable results. In the limit of  $\kappa/\Omega \rightarrow 2.0$ , the effect of horseshoe dominant encounters would always dominate and  $N$ -body simulations always show  $\langle i_*^2 \rangle^{1/2} / \langle e_*^2 \rangle^{1/2} \simeq 1$ .

In summary, the results of  $N$ -body simulation are consistent with the results in section 2. Therefore, the physical argument in section 2 (mainly with quantities before velocity averaging,  $P_{\text{heat}}$  and  $Q_{\text{heat}}$ ) would be valid.

#### 4 CONCLUSIONS

We have studied the ratio of the velocity dispersion ( $\sigma_z/\sigma_R$ ) which is attained through mutual gravitational interaction among bodies in disc potentials. We examined the cases with Kepler rotation  $\kappa/\Omega = 1$  to solid-body rotation  $\kappa/\Omega = 2$ ,

where  $\kappa$  and  $\Omega$  are the epicycle and circular frequencies. Another parameter  $\nu/\Omega$  does not affect the result, because shear motion of particles, which is the origin of the anisotropic velocity dispersion, is independent of  $\nu/\Omega$ . We employed two different numerical methods, statistical compilation of two-body encounters (section 2) and  $N$ -body simulations (section 3). With the former method the physical properties are clearer and wider parameter range can be examined, while the results are not direct and some assumptions are introduced in the statistical compilation. On the other hand, the latter method is direct, although parameter range we can simulate is restricted by cpu time. The combination of the complementary methods would enable us to derive conclusive results.

We found that the ratio becomes the equilibrium state much more quickly than the amplitude of the velocity dispersion changes except when  $\kappa/\Omega$  is near 1. The equilibrium ratio depends on amplitude of velocity dispersion and disc potential parameter,  $\kappa/\Omega$ . We found three characteristic velocity regimes:

$$\left\{ \begin{array}{l} \text{the shear dominant region:} \quad e \lesssim \alpha/\sqrt{2}, \\ \text{the horseshoe dominant region:} \\ \quad \alpha/\sqrt{2} \lesssim e \lesssim (\kappa/\Omega)\alpha^{-1/3}, \\ \text{the dispersion dominant region:} \quad (\kappa/\Omega)\alpha^{-1/3} \lesssim e, \end{array} \right. \quad (25)$$

where  $\alpha = 4 - \kappa^2/\Omega^2$  and  $e$  corresponds to the amplitude of the random velocity of the relative motion of two particles normalized by  $r_g\Omega$ . The velocity dispersion  $\sigma_R$  and  $e$  are related as  $\langle e^2 \rangle^{1/2} = 2\sigma_R/(r_g\Omega)$  for a system of identical particle or  $\langle e^2 \rangle^{1/2} = \sqrt{2}\sigma_R/(r_g\Omega)$  for a system with large mass ratio such as stars and giant molecular clouds (see Eqs. (8) and (16)). The characteristic radius  $r_g$  is defined by Eq.(2) and it is related to tidal radius  $r_t$  as  $r_g = \alpha^{1/3}r_t$ .

In the shear dominant region, shear motion dominates epicycle motion. Since shear motion is horizontal and orbits are bent before the bodies come close to each other, gravitational scattering takes place two-dimensionally. As a result, only  $\sigma_R$  is raised so that  $\sigma_z/\sigma_R \ll 1$ . In the dispersion dominant region, epicycle velocity is so large that orbits

are not perturbed until they closely approach each other. The close encounters are well approximated by Rutherford formula neglecting tidal force, as Lacey(1984) and IKM93 did. As explained in section 2, energy equipartition in horizontal and vertical motion at the close encounters and the deceleration in horizontal velocity by shear motion lead to excessive  $\sigma_R$ . IKM93 predicted  $\sigma_z/\sigma_R = 0.5-0.8$  ( $\sigma_z/\sigma_R$  is smaller for smaller  $\kappa/\Omega$ ). Our numerical simulations agree with IKM93's prediction for relatively small  $\kappa/\Omega$  and suggest agreement even for larger  $\kappa/\Omega$ . However, dispersion dominant region, where IKM93's prediction is valid, is overwhelmed by the newly found horseshoe dominant region in velocity space in the case of  $\kappa/\Omega \sim 2$  (See (25)). In the horseshoe dominant region, 'horseshoe'-type close encounters dominates gravitational relaxation. In this case,  $\sigma_z/\sigma_R \sim 1$  is predicted. The physical reason for  $\sigma_z/\sigma_R \sim 1$  is given in section 2. Due to the contamination from the encounters in other velocity regimes (the particles velocities have Rayleigh distribution),  $N$ -body simulations usually show  $\sigma_z/\sigma_R$  smaller than 1. However,  $\sigma_z/\sigma_R \sim 1$  is actually shown in the case of  $\kappa/\Omega \sim 2$  as in Fig. 14 because the contamination diminishes as  $\kappa/\Omega \rightarrow 2$ .

In Fig. 15, we draw a schematic figure on the ratio of velocity dispersion of self-gravitating particles in disc potentials from Kepler rotation to solid-body rotation. The boundaries of the three regions are given by the relation (25). In reality, the velocity distribution of particles makes the boundaries obscured through the averaging on the Rayleigh distribution.

## ACKNOWLEDGMENTS

We thank Hiroyuki Emori and Hidekazu Tanaka for fruitful discussion and for useful comments on the numerical codes. We also thank Kiyoshi Nakazawa for continuous encouragement.

## REFERENCES

- Barbanis B., Woltjer L., 1967, ApJ, 150, 461  
 Binney J., Lacey C., 1988, MNRAS, 230, 597  
 Binney J., Tremaine S., 1987, Galactic Dynamics. Princeton Univ. Press, Princeton, New Jersey.  
 Brown E. W., 1911, MNRAS, 71, 438  
 Chandrasekhar S., 1949, Principles of Stellar Dynamics. Yale Univ. Press, New Haven, CN.  
 Chen B., Asiain R., Figueras F., Torra J., 1997, A&A, 318, 29  
 Emori H., Ida S., Nakazawa K., 1993, PASJ, 45, 321  
 Hasegawa M., Nakazawa K., 1990, A&A, 227, 619  
 Hénon M., Petit J.-M., 1986, Celes. Mech. 38, 67  
 Icke V., 1982, ApJ, 254, 517  
 Ida S., 1990, Icarus, 88, 129  
 Ida S., Kokubo E., Makino J. 1993, MNRAS, 263, 875 (IKM93)  
 Ida S., Makino J., 1992a, Icarus, 96, 107  
 Jenkins A., Binney J., 1990, MNRAS, 245, 305  
 Kokubo E., Ida S., 1992, PASJ, 44, 601  
 Lacey C., 1984, MNRAS, 208, 687 (L84)  
 Lacey C., 1991, in Sundelius B., ed., Dynamics of Disk Galaxies. Dept. of Astronomy/Astrophysics, Göteborg Univ., Sweden, P.257  
 Lissauer J. J., Stewart G. R., 1993, Protostars and Planets III, Univ. of Arizona Press, Tucson, P.1061  
 Makino J., 1991, PASJ, 43, 859  
 Makino J., Aarseth S. J., 1992, PASJ, 44, 141  
 Makino J., Kokubo E., Taiji M., 1993, PASJ, 45, 349  
 Makino J., Taiji M., Ebisuzaki T., Sugimoto D., 1997, ApJ, 480, 432  
 Ohtsuki K., 1998, Icarus, in press  
 Petit J.-M., Hénon M., 1986, Icarus, 66, 536  
 Press W. H., Flannery B. P., Teukolsky S. A., Vetterling W. T., 1986, Numerical Recipes. Cambridge Univ. Press, London/New York.  
 Spitzer L., Schwarzschild M., 1953, ApJ, 118, 106  
 Stewart G. R., Wetherill G. W., 1988, Icarus, 74, 542  
 Stewart G. R., Ida S., 1998, Icarus, in press  
 Tanaka H., Ida S., 1996, Icarus, 120, 371  
 Villumsen J. V., 1985, ApJ, 290, 75  
 Wielen R., 1977, A&A, 60, 263

## APPENDIX A:

We evaluate the time-scale for the equilibrium state of  $i/e$  to be realized and that for the random energy ( $e^2 + i^2$ ) to be increased in the dispersion dominant region. The former is defined by

$$T_{\text{ratio}} = \left[ \frac{e}{i} \frac{d(i/e)}{dt} \right]^{-1}, \quad (\text{A1})$$

and the latter is

$$T_{\text{random}} = \left[ \frac{1}{e^2 + i^2} \frac{d(e^2 + i^2)}{dt} \right]^{-1}. \quad (\text{A2})$$

Accordingly,  $T_{\text{ratio}}$  and  $T_{\text{random}}$  are obtained from change rates of  $e^2$  and  $i^2$ . When  $e$  and  $i$  are large enough that the impulse approximation is valid, they are written as (Ida et al. 1993, Tanaka & Ida 1996):

$$\begin{cases} \frac{de^2}{dt} = C \left[ (1 + \xi^2)K(\lambda) - \frac{3e^2}{i^2 + \xi^{-2}e^2}E(\lambda) \right], \\ \frac{di^2}{dt} = C \left[ K(\lambda) - \frac{3i^2}{i^2 + \xi^{-2}e^2}E(\lambda) \right], \end{cases} \quad (\text{A3})$$

where  $K$  and  $E$  are the complete elliptic integral of the first and second kind,  $\xi = 2\Omega/\kappa$ , and  $\lambda^2 = (1 - \xi^{-2})e^2/(e^2 + i^2)$ . The factor  $C$  is defined by

$$C = \frac{4}{\pi} \frac{\nu}{\Omega} n_s \left[ \ln(1 + \Lambda^2) - \frac{\Lambda^2}{1 + \Lambda^2} \right] \frac{1}{i\sqrt{e^2 + i^2}} \quad (\text{A4})$$

From Eqs. (A1), (A2), and (A3), We can rewrite  $T_{\text{ratio}}$  and  $T_{\text{random}}$  as

$$\begin{cases} T_{\text{ratio}} = \frac{e^2 + i^2}{C} \left\{ \left[ \frac{e}{i} - \frac{i}{e}(1 + \xi^2) \right] K(\lambda) \right\}^{-1}, \\ T_{\text{random}} = \frac{e^2 + i^2}{C} \\ \times \left[ (2 + \xi^2)K(\lambda) - 3 \left( \frac{e^2 + i^2}{i^2 + \xi^{-2}e^2} \right) E(\lambda) \right]^{-1}. \end{cases} \quad (\text{A5})$$

In above equations, when the non-dimensional factors multiplied to  $(e^2 + i^2)/C$  are order unity, it is easy to see both  $T_{\text{ratio}}$  and  $T_{\text{random}}$  are the same order as the Chandrasekhar's two body relaxation time. In the case where the disc potential is close to that of solid-body rotation ( $\xi \rightarrow 1$  or  $\kappa/\Omega \rightarrow 2.0$ ), however,  $T_{\text{random}}$  tends toward infinity, while  $T_{\text{ratio}}$  does not (we consider the case where particles have not reach the state of the equilibrium ratio yet). In Fig.

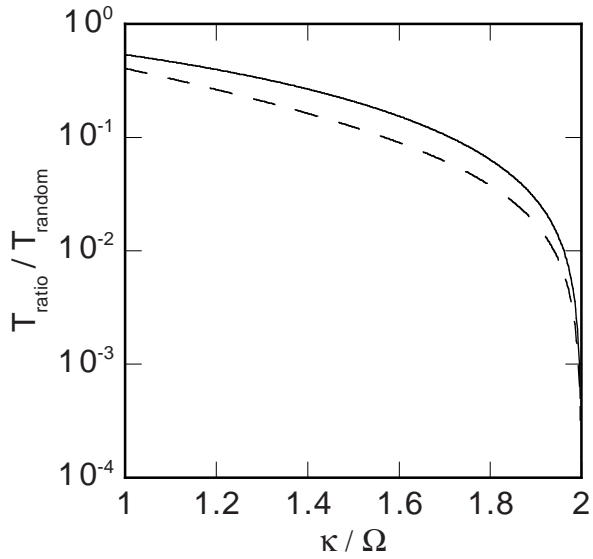


**Figure A1.** The ratio between  $T_{\text{ratio}}$  and  $T_{\text{random}}$  against  $\kappa/\Omega$ . The solid line and the dashed line correspond to  $i/e = 1.0$  and  $2.0$ .

A1,  $T_{\text{ratio}}/T_{\text{random}}$  as a function of  $\kappa/\Omega$  is plotted in the cases where  $i/e = 1.0$  and  $2.0$  (note that  $T_{\text{ratio}}/T_{\text{random}}$  is a function of  $i/e$ , but not  $e$  nor  $i$ ). When  $\kappa/\Omega$  is nearly 1 ( $\xi \sim 2$ ),  $T_{\text{ratio}}$  and  $T_{\text{random}}$  are the same order. On the other hand, when  $\kappa/\Omega$  is nearly 2 ( $\xi \sim 1$ ),  $T_{\text{random}}$  is much larger than  $T_{\text{ratio}}$ . In the latter case, disc heating proceeds quasi-stationarily compared to the process to reach the state of the equilibrium ratio.